nuclear fusion
IAEA

PAPER • OPEN ACCESS

Double-null power-sharing dynamics in MAST-U

To cite this article: B. Kool *et al* 2025 *Nucl. Fusion* **65** 106032

OPEN ACCESS
IOP Publishing | International Atomic Energy Agency
Nuclear Fusion
Nucl. Fusion **65** (2025) 106032 (28pp)
https://doi.org/10.1088/1741-4326/ae04fe

Double-null power-sharing dynamics in MAST-U

B. Kool[1,2,*], T.M. van den Doel[1,3], G.L. Derks[1,2], S.S. Henderson[4], J. Lovell[5], O.P. Bardsley[4], M. Lafferty[4], T.A. Wijkamp[1], P.A. Figueiredo[1], S. Silburn[4], A. Tookey[4], R. Scannell[4], N. Lonigro[4,6], J.M. Stobbs[4], L. Kogan[4], K. Verhaegh[3,4], M. van Berkel[1,7] and the MAST-U Team[a]

[1] DIFFER—Dutch Institute for Fundamental Energy Research, Eindhoven, Netherlands
[2] Department of Mechanical Engineering, Eindhoven University of Technology, Eindhoven, Netherlands
[3] Department of Applied Physics, Eindhoven University of Technology, Eindhoven, Netherlands
[4] United Kingdom Atomic Energy Authority, Culham Campus, Abingdon, United Kingdom of Great Britain and Northern Ireland
[5] Oak Ridge National Laboratory, Oak Ridge, TN, United States of America
[6] York Plasma Institute, University of York, York, United Kingdom of Great Britain and Northern Ireland
[7] Department of Electrical Engineering, Eindhoven University of Technology, Eindhoven, Netherlands

E-mail: b.kool@differ.nl

Received 11 June 2025, revised 13 August 2025
Accepted for publication 9 September 2025
Published 24 September 2025

Abstract

Maintaining an effective double-null (DN) configuration is expected to be challenging in reactor-scale tokamak devices. As divertor power-sharing is closely linked to the magnetic topology, even minor variations can lead to fast power-sharing fluctuations which exacerbate the already daunting exhaust challenge. While the static aspects of DN power-sharing have been extensively studied across various devices, this paper presents the first detailed investigation of its dynamic behaviour. We employ dedicated H-mode experiments in MAST-U, in Super-X divertor configuration, featuring perturbation frequencies up to 200 Hz. Our results clearly show no significant dynamic damping of the power-sharing within this frequency range: the divertor responds equally to both fast and slow perturbations. Moreover, the dynamic response also aligns with quasi-static results from slow ramps, implying that static power-sharing models remain valid even for fast fluctuations. Occasionally, some deviations from the otherwise mainly linear behaviour are observed, alongside notable scatter and asymmetries between upwards and downwards trajectories. These observations are likely linked to changes in core conditions, though the underlying mechanisms remain unclear and require further study.

Keywords: power-sharing, dynamic double-null, tokamak exhaust, system identification, divertor

(Some figures may appear in colour only in the online journal)

[a] See Harrison *et al* 2024 (https://doi.org/10.1088/1741-4326/ad6011) for the MAST-U Team.
[*] Author to whom any correspondence should be addressed.

1. Introduction

One of the most critical challenges on the path to fusion energy is the power exhaust challenge. If left unmitigated, the heat and particle loads in the divertor region are predicted to greatly exceed the material limits of presently available materials for reactor-scale devices [1–3]. To reduce the target loads to manageable levels, operation in the detached plasma regime is required, maintained through active exhaust control systems [1–5].

The exhaust challenge is compounded in the recently emerging compact reactor designs like STEP [4, 6, 7] and SPARC/ARC [8, 9] which aim to provide a faster and more cost-effective path to the commercial deployment of fusion energy [10–12]. In these compact designs, the physical area available for power deposition is significantly reduced, exacerbating the already formidable exhaust challenge faced in conventional reactors such as ITER and DEMO. For example, assuming comparable divertor designs and upstream conditions, the unmitigated heat flux in STEP is estimated to be roughly twice as high on the outer divertor and three times higher on the inner divertor relative to DEMO [3].

To mitigate these risks, alternative divertor configurations (ADCs) which rely on plasma shaping to improve the power exhaust have gained attention lately, including the Super-X configuration [13–15]. Also, highly radiative plasma regimes like the *X*-point radiator [16, 17] might be employed to reduce the demands on the divertor. Furthermore, double-null (DN) configurations are increasingly considered for fusion power reactors (e.g. STEP [18], ARC [19], and DEMO [20, 21]) to improve power distribution.

A DN equilibrium features two magnetic nulls, as depicted in figure 1(*b*). In a fully connected DN, the inboard and outboard scrape-off layers (SOLs) are magnetically disconnected. In addition to distributing the power to a second divertor set, these equilibria ease the burden of power exhaust by directing the majority of the power towards the outer targets [22]. This is especially promising for compact, spherical, reactor designs as their small radius implies a vulnerable inner target due to the reduced surface area. The lack of available physical space on the inboard side of compact devices restricts the application of mitigation strategies, in contrast, the outer divertors are located at large major radius. Here, in addition to favourable surface area scaling, more physical space is available to implement mitigation strategies like ADCs [23, 24]. DN configurations are therefore a prime candidate for compact, spherical, reactor designs.

In practice, a fully connected DN configuration in which the inner and outer SOLs are completely disconnected cannot be maintained as the magnetic control precision is limited. Therefore, some degree of disconnection towards lower double-null (LDN) or upper double-null (UDN) will always be present, see figure 1. Maintaining an effective DN configuration (i.e. close enough to a connected DN) however still requires precise magnetic control [4, 26]. The connectedness is commonly parametrised by ΔR_{sep}, the distance between the two magnetic separatrices as measured at the outer midplane. A double null configuration is typically considered connected for

$$|\Delta R_{\text{sep}}| \leqslant \frac{\lambda_q}{2}, \tag{1}$$

with λ_q the heat load SOL e-folding width [27–29].

The vertical plasma position Z heavily influences ΔR_{sep} and therefore how much the configuration deviates from a fully connected DN [26, 27]. As the vertical position is inherently unstable, it has to be controlled actively [30, 31]. For reactor-scale devices, λ_q is expected to be millimetre sized [3, 32]. Combined with the additional challenges of magnetic control in an activated reactor vessel [33], maintaining an effective DN configuration is therefore challenging for fusion power reactors. This implies that significant oscillations in Z and therefore ΔR_{sep} can be expected, leading to significant power-sharing fluctuations. This is especially concerning for spherical designs as their high elongation further amplifies the vertical control challenge [4, 26, 27, 34].

Fluctuations in the power flowing towards the divertor region have to be compensated through active exhaust control systems [2, 4, 5, 35, 36]. These systems typically rely on relatively slow actuators, such as gas valves, to increase the divertor neutral pressure and impurity concentration, thereby increasing divertor power mitigation. This entails that fast perturbations ($\gg 1$ Hz) cannot be adequately corrected for with the currently foreseen actuator set. Power-sharing fluctuations arising from vertical control can occur on very short timescales ($>$100 Hz), making them particularly concerning in the development of effective exhaust control systems.

Therefore, to achieve suitable vertical control and exhaust control for future fusion power plants, the power-sharing dynamics w.r.t. ΔR_{sep} have to be understood. Such power-sharing effects might be exploited deliberately, as considered in the dynamic double null scenario for STEP [37]. Rather than constantly trying to maintain a fully connected DN, the dynamic DN scenario constitutes purposefully oscillating ΔR_{sep}. The power-sharing dynamics may enable access to effective power-sharing beyond the allowable static ΔR_{sep} range defined by equation (1); that is, the plasma is moved back towards a connected DN before the divertor has time to respond. Power-sharing dynamics might therefore dampen the effective heat load experienced by the divertor and could be key to combining the strict target load limits with the challenging vertical control situation for fusion power reactors.

The power-sharing has been elaborately studied (quasi)-statically on DIII-D [38], MAST [39–41], EAST [42], Alcator C-Mod [28], TCV [29], and WEST [43]. It was found that plasma drift effects lead to asymmetric up-down power sharing [40, 41, 44]. Therefore, a deliberate disconnection is required to compensate this and achieve balanced power loading. For example, a 2 cm up-shift was found to result in balanced up-down power sharing in MAST [39, 41] with $\mathbf{B}\times\nabla B$ pointing towards the lower divertor while a down-shift is required in DIII-D ($\Delta R_{\text{sep}} = -6$ to -25 mm) with $\mathbf{B}\times\nabla B$ pointing towards the upper divertor [45].

The *static* power-balance in MAST-U has been investigated recently [46]. Additionally, the detachment onset and reattachment times in MAST-U have been examined in a separate *static* study [47]. In this paper, we present the first analysis of DN power-sharing *dynamics*, using dedicated experiments in MAST-U employing high confinement-mode (H-mode) and the Super-X divertor configuration.

We first discuss the experimental setup in section 2. Proceeding to our experimental results, we first discuss the linearity of the divertor response in section 3, followed by an analysis of the power-sharing dynamics in section 4. We discuss our results in section 5 and present our conclusions in section 6.

2. Experimental setup

In this section, we discuss the setup of the dynamic power-sharing experiments at the MAST-U tokamak. We cover the plasma scenario, actuation and measurement of ΔR_{sep}, the design of the perturbation signals, and the considered diagnostics. We end this section with a brief introduction to frequency domain analysis as a background for the discussion of our experimental results.

2.1. Plasma scenario

MAST-U is a medium-sized ($R = 0.7$ m), low aspect ratio ($R/a = 1.4$), spherical tokamak in the UK [48]. It features a fully up-down symmetric magnetic coil set, designed to run in DN configuration. MAST-U has been especially designed to study ADCs through its extensive magnetic shaping capabilities. It uniquely integrates these ADCs with strong divertor baffling to further improve the power-exhaust. All experiments considered in this work feature the Super-X divertor configuration, see figure 1.

All considered experiments are run in H-mode. In this scenario, the core density is generally increasing throughout each shot, ranging from 1.8 to 2.2×10^{20} m^{-3}. This leads to a build-up in divertor neutral pressure, amplified by the strong divertor baffling and the absence of cryopumping in these experiments. Fuelling occurs through the high-field-side main chamber deuterium gas valve.

Our experiments employ Neutral-Beam Injection (NBI), using both the on-axis and off-axis systems, each delivering 1.5 MW. However, as will be discussed in section 2.2, we apply power-sharing perturbations by perturbing the plasma vertical position. This implies that the coupling efficiency from beam to plasma can change throughout the shot as the beam intersects more or less of the core plasma depending on the vertical position. The total power deposition into the core therefore fluctuates significantly during a perturbation (e.g. 0.1–0.2 MW per NBI for #48648). This results in separatrix power (P_{sep}) fluctuations in addition to the applied power-sharing perturbations (e.g. 0.3–0.5 MW for #48648). See appendix A for more details.

In these experiments, the core plasma exhibits significant magneto-hydrodynamic (MHD) activity. This is illustrated in appendix A. Aside from terminating most discharges early through MHD mode locking, this MHD activity also results in P_{sep} fluctuations in addition to the applied power-sharing perturbations. Some discharges exhibit Edge Localised Modes (ELMs) [49], while others are predominantly ELM-free. The ELMs are filtered out in post-processing, as detailed in appendix C.

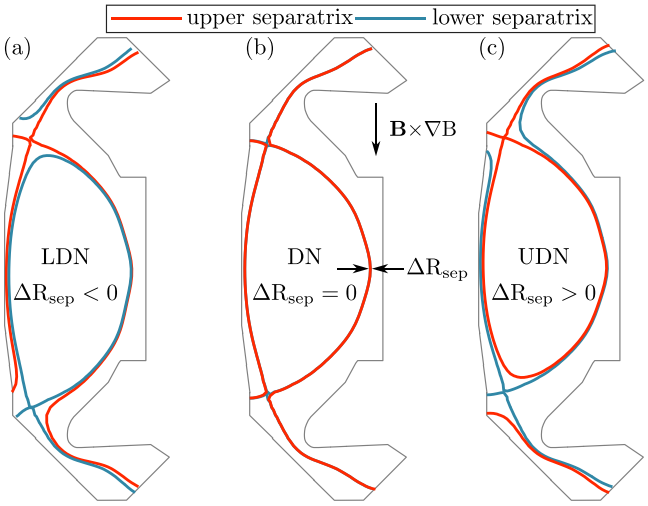

Figure 1. Magnetic double-null equilibria in MAST-U. (*a*) Lower double-null (LDN), (*b*) A fully connected double-null (DN), (*c*) upper double-null (UDN). ΔR_{sep} is defined as the inter-separatrix distance at the outer midplane. The direction of the $\mathbf{B} \times \nabla B$ drift is indicated as downwards with $\mathbf{B}$ pointing out of the page [25].

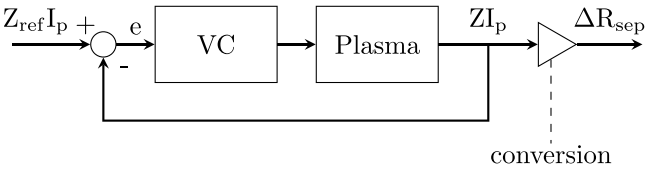

Figure 2. Schematic overview of the MAST-U vertical control system. To actuate ΔR_{sep} a sinusoidal perturbation trace is applied to the vertical controller reference Z_{ref}. The resulting ZI_{p} signal is subsequently converted to ΔR_{sep}, see section 2.2 and appendix D.

2.2. ΔR_{sep} actuation and measurement

The power-sharing is perturbed by actuating ΔR_{sep}, in line with static studies [28, 29, 38, 39, 42]. As ΔR_{sep} cannot be controlled directly, we actuate ΔR_{sep} by perturbing the vertical control system reference Z_{ref}. The control system estimates ZI_{p} as the combined plasma current (I_{p}) and vertical position (Z) signal from magnetic sensors [50]. The measured value is compared to the reference value to generate an error signal as $e = Z_{\text{ref}} I_{\text{p}} - ZI_{\text{p}}$. The vertical control system then adjusts the vertical control coil currents to minimise the position error through a proportional-derivative (PD) controller. A schematic overview of the vertical control system is shown in figure 2.

Since ΔR_{sep} is perturbed through the vertical control system reference Z_{ref}, the vertical control system performance influences the ultimately applied ΔR_{sep} perturbation. In this work, we consider sinusoidal perturbations in the 40–200 Hz

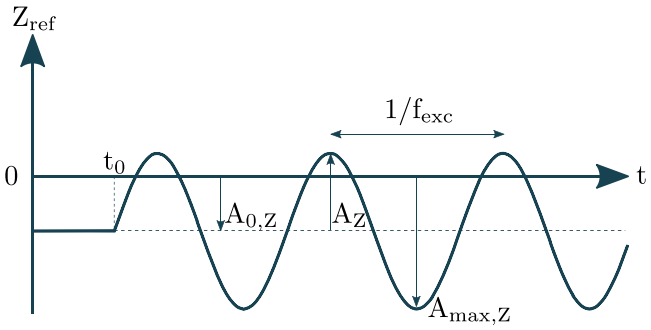

Figure 3. Definition of each of the perturbation parameters with starting time t_0, excited frequency f_{exc}, amplitude A_Z, offset w.r.t the magnetic centre $A_{0,Z}$, and maximum achieved deviation $A_{\mathrm{max},Z}$. We show the Z_{ref} signal, according to equation (2). The equivalent parameters can also be expressed in ΔR_{sep} as $A_{\Delta R_{\mathrm{sep}}}$, $A_{0,\Delta R_{\mathrm{sep}}}$, and $A_{\mathrm{max},\Delta R_{\mathrm{sep}}}$.

range. Although minor deviations from the requested pure sine waves can sometimes be observed, especially for the highest frequencies, the vertical control system performance was deemed satisfactory for all experiments, see also appendix D.

In MAST-U, ΔR_{sep} cannot be measured directly but is extracted from the magnetic equilibrium reconstruction code EFIT++ [51, 52]. Dedicated, high time resolution EFIT++ reconstructions have been made available for these experiments at 1 kHz. Since ΔR_{sep} and Z are approximately proportionally related [26, 27], we can also use Z as a fast proxy for ΔR_{sep}. We extract Z from the vertical control signal ZI_{p} by dividing by the plasma current. Scaling and shift factors are tuned to ensure that the scaled Z measurement matches the EFIT++ ΔR_{sep} measurement, see appendix D. The resulting ΔR_{sep} signal is available at 1 MHz sampling frequency.

2.3. Perturbation signal design

The perturbation signals selected for Z_{ref} are pure sine waves, therefore, we only identify the system dynamics at one frequency point per perturbation signal. Although signals consisting of multiple frequencies (i.e. multi-sines) have successfully been employed in various tokamak system identification experiments [35, 53–55], we opt for pure sine waves since: (1) this improves the signal-to-noise ratio (SNR) [56], (2) makes the Z_{ref} trace as easy as possible to follow for the vertical control system and therefore minimises the introduced error, and (3) the relatively high perturbation frequencies (40–200 Hz) imply that the required timespan to achieve any number of periods is rather short, therefore, multiple frequencies can be identified in a single experiment by dividing it in sequential time sections in which different perturbation signals are applied.

The Z_{ref} trace for each perturbation in this study is described by

$$Z_{\mathrm{ref}} = A_{0,Z} + A_Z \sin\left(2\pi f_{\mathrm{exc}}\left(t - t_0\right)\right), \tag{2}$$

with offset A_0 [cm], amplitude A_Z [cm] and excited frequency f_{exc} [Hz] (see figure 3). The perturbation starts at $t = t_0$. Note that, in this description, we consider the vertical position as measured by the vertical control system. This does not necessarily align with the actual vertical position through offsets and drifts of magnetic sensors, see appendix D. Furthermore, $A_{0,Z} = 0$ refers to a magnetically balanced configuration. Note that this does not fully coincide with the point where the up-down power-sharing is symmetric as discussed in section 1.

An overview of the applied perturbations for each shot is shown in table 1, including the observed ΔR_{sep} for each perturbation. This includes the maximum deviation from a magnetically balanced configuration defined as $A_{\mathrm{max},\Delta R_{\mathrm{sep}}} = |A_{0,\Delta R_{\mathrm{sep}}}| + |A_{\Delta R_{\mathrm{sep}}}|$, see figure 3. The applied perturbations have been designed to respect the vertical control system limits, this is explored in appendix E. For an amplitude of 4 cm, 200 Hz was observed to be the maximum allowable perturbation frequency where the vertical control system still adequately tracks the specified reference. The lowest considered frequency is 40 Hz since previous system identification experiments, predominantly using gas perturbations, found no dynamics within the SOL up to this frequency across several devices [57], likely due to the fast parallel transport in the SOL. The amplitude ranges from 1–6 cm in A_Z, corresponding to 1–10 mm in $A_{\Delta R_{\mathrm{sep}}}$.

Both balanced ($A_{0,Z} = 0$) and down-shifted ($A_{0,Z} < 0$) perturbations have been used. Up-shifted perturbations ($A_{0,Z} > 0$) were not possible due to operational constraints.

2.4. Measurements

In this work, we consider various diagnostics to build an overarching picture of the power-sharing dynamics. Only diagnostics with relatively high acquisition rates have been selected for our analysis, considering the applied perturbations are in the 40–200 Hz frequency range. The Balmer-alpha emission is monitored using various D-alpha filterscopes and the D-alpha—filtered high-speed video (HSV) system. The peak target heat flux is measured with infrared (IR) cameras. The D_2 Fulcher-band emission, used as a proxy for ionisation [24, 58, 59], is obtained from the fast spectroscopy system (ultra-fast divertor spectroscopy or UFDS) and spectral imaging (MWI + XPI). From the latter, we extract both the target intensity (I_{sp}) and the distance to the X-point (L_x). Additionally, we consider the core electron density from interferometry (IF). The divertor target coverage and acquisition frequency of each diagnostic is listed in table 2. For more details on the diagnostics, see appendix B.

The applied Z_{ref} perturbations were observed to also affect the divertor magnetic configuration. The diagnostics sightlines were adapted to minimise the effect of this movement on the measurements, this is detailed in appendix B.

The H-mode scenario considered in these experiments occasionally exhibits ELMs, as discussed in section 2.1, affecting the diagnostic signals. Since this disturbance is mostly non-periodic, the ELMs distort any frequency domain analysis, particularly for high frequencies where there are less datapoints per period. Therefore, the diagnostic data during ELMs is replaced through linear interpolation. The ELMs are also used as reference points in timing corrections required for

Table 1. Perturbation parameters of all shots considered in this work, subdivided into perturbation sections indicated by letters. We list the perturbation frequency f [Hz], perturbation offset $A_{0,Z}$ [cm] and perturbation amplitude A_Z [cm]. This is expressed in ΔR_{sep} as $A_{0,\Delta R_{\mathrm{sep}}}$ [mm] and $A_{\Delta R_{\mathrm{sep}}}$ respectively. Additionally, $A_{\mathrm{max},\Delta R_{\mathrm{sep}}} = |A_{0,\Delta R_{\mathrm{sep}}}| + |A_{\Delta R_{\mathrm{sep}}}|$ [mm] indicates the maximum deviation from a magnetically balanced configuration, see figure 3.

Shot	f_{exc} [Hz]	$A_{0,Z}$ [cm]	A_Z [cm]	$A_{0,\Delta R_{\mathrm{sep}}}$ [mm]	$A_{\Delta R_{\mathrm{sep}}}$ [mm]	$A_{\mathrm{max},\Delta R_{\mathrm{sep}}}$ [mm]
4848a	40	−2	3	−2.0	4.7	6.7
4848b	40	−4.5	5.5	−5.7	9.5	15.2
48652	80	−3	4	−3.1	7.2	10.3
48900	80	−2	3	−2.0	4.5	6.5
48909	120	−2	3	−2.3	4.3	6.7
49058a	200	−2	3	−2.2	3.2	5.3
49058b	120	−2	3	−2.2	4.0	6.2
49059a	200	0	4	0.4	4.6	4.9
49059b	80	0	4	0	5.7	5.7
49062a	120	0	1	0.8	1.3	2.1
49062b	120	0	2	0.4	2.9	3.4
49062c	120	0	3	0.2	4.2	4.4
49260a	120	0	4	0.6	6.0	6.6
49260b	120	0	5	0.8	7.4	8.2
49260c	120	0	6	0.7	7.2	7.8
49260d	160	0	4	0.8	4.0	4.9
49261a	120	0	4	0.5	6.3	6.8
49261b	120	0	5	0.4	6.8	7.2
49261c	120	0	6	0.5	6.2	6.7
49261d	160	0	4	0.6	4.2	4.7

Table 2. Target coverage and acquisition frequency f_{a} of all measurements employed in this study. See also appendix B.

	Diagnostic	Inner L	Inner U	Outer L	Outer U	f_{a}
■	Interferometry (IF)	✘	✘	✘	✘	100 kHz
■	D-alpha scopes	✘	✘	✓	✓	100 kHz
■	High-speed video (HSV)	✓	✓	✘	✘	1 kHz
■	IR cameras	✘	✘	✓	✓	0.4 or 1.25 kHz
■	UFDS	✘	✘	✓	✘	100 kHz
■	L_{x}, MWI Front position	✘	✘	✓	✘	400 Hz
■	I_{sp}, MWI and XPI strike-point intensity	✓	✘	✓	✘	400 Hz

some diagnostics. Both this time correction and ELM filtering are discussed in appendix C.

2.5. Frequency domain analysis

The analysis of the power-sharing dynamics presented in this paper mainly considers the frequency domain as it can provide a comprehensive understanding of a system's behaviour. Recently, such a frequency domain approach has already been applied to investigate and control the core and divertor dynamics of multiple tokamaks [35, 53–55]. In this paper, we apply this approach to power-sharing dynamics for the first time.

The transformation from the time domain (t) to the frequency domain (f) is achieved through the discrete Fourier transform (DFT) $\mathcal{F}$ as

$$U(f) = \mathcal{F}(\mathrm{u}(t)), \tag{3}$$

$$Y(f) = \mathcal{F}(y(t)), \tag{4}$$

with the input $u(t)$ and output $y(t)$ in time domain and their frequency domain counterparts as $U(f)$ and $Y(f)$. In our case, $u(t)$ is always $\Delta R_{\mathrm{sep}}(t)$ while $y(t)$ can be any given diagnostic measurement.

The application of the DFT is schematically illustrated in figure 4(a). Here, we also illustrate how the linearity of a system can be identified through the DFT: when perturbing a fully linear system, the output response is only observed on the excited frequency f_{exc}. However, for a smooth non-linear system, a response is also observed on integer multiples of f_{exc} [60, 61]. This effect is employed to analyse the linearity of the power-sharing dynamics in section 3. We characterise the linearity of the response through the harmonic distortion ratio (HDR), defined as

$$\mathrm{HDR} = \frac{|Y_{2f_{\mathrm{exc}}}|}{|Y_{f_{\mathrm{exc}}}|}, \tag{5}$$

with $Y_{f_{\mathrm{exc}}}$ and $Y_{2f_{\mathrm{exc}}}$ as the frequency domain response at the excited frequency and first harmonic respectively.

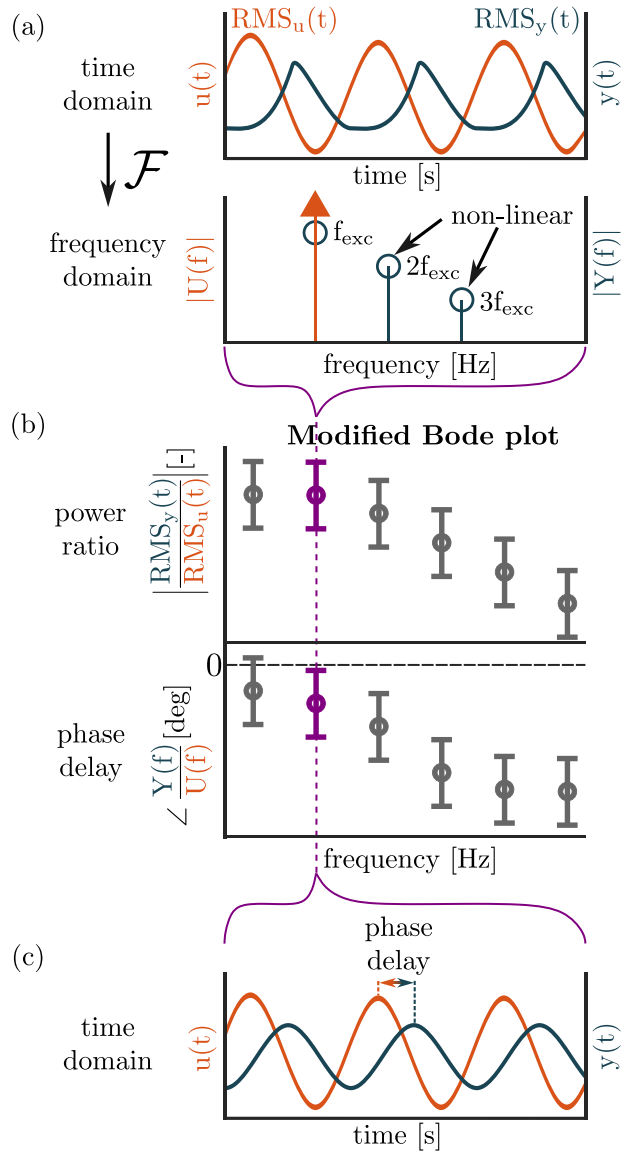

Figure 4. Schematic illustration of the employed frequency domain analysis. (*a*) Input u (ΔR_{sep}) and output y (diagnostic signal) in time domain (upper) and frequency domain (lower) with the root-mean-square (RMS) as a measure for signal power. Non-linear contributions are evidenced as harmonics of the excited frequency f_{exc}. (*b*) Modified Bode plot of the input-to-output dynamics in frequency domain, showing the power (RMS) ratio with the phase delay describing only linear components. We illustrate a decreasing magnitude and increasing phase delay with frequency. (*c*) Time domain representations of the input and output signals of a single frequency point from the Bode plot (purple).

In this paper, we employ the local polynomial method (LPM) [61, 62] to correct for distortions in the DFT which arise from drifts and slow transients. The error bars shown in the Bode plots in this paper also result from the LPM.

To analyse a system's response in frequency domain, Bode diagrams are typically used to represent the linear response around an operating point by showing the magnitude and phase response across frequency [63]. However, in our analysis, we consider a modified Bode plot in which we show the power ratio of the input signals instead of the more commonly used magnitude ratio. We make this choice to better accommodate non-linear effects into our analysis. This is required since significant non-linear effects are occasionally observed, as will be discussed in section 3. Our approach is conceptually illustrated in figure 4(*b*). We plot the power ratio and phase delay between the input and output signals for each frequency, the time domain representation of which is shown in figure 4(*c*). Note that the phase delay still only considers the linear response. The experiment is repeated with different perturbation frequencies to identify the frequency response of the system. We define the power ratio of the input and output signals as the root-mean-square (RMS) ratio of the input and output. The RMS is often considered as a measure of the signal power [63], irrespective of the linearity of the response, defined as

$$\mathrm{RMS} = \sqrt{\frac{1}{N}\sum_{n=1}^{N} x_n^2}, \tag{6}$$

with N as the number of samples in the signal x.

In the next section, we start the data analysis of our experiments by exploring the linearity of the observed response.

3. Linearity

Across all experiments, we observe responses ranging from dominantly linear to dominantly non-linear. In this section, we examine this behaviour in detail, followed by a discussion, and conclude with the implications of these non-linear effects for the power-sharing analysis.

3.1. Observations

In our experiments, the *upper-outer* divertor exhibits a significantly more linear response compared to the *lower-outer* divertor. Also, we observe smaller differences between upwards and downwards trajectories for the *upper-outer* divertor, showing a significantly cleaner response. This is illustrated in figure 5, showing the D-alpha filterscope responses for #49059b. First, we consider the response of the *upper-outer* divertor, see figure 5(*a*) for the time domain (upper) and frequency domain (lower) response. The applied ΔR_{sep} perturbation is overlayed in black. It can be observed that the response contains no input frequency harmonics which exceed the noise floor, consequently, we conclude that the response is dominantly linear. This is also evidenced through the relatively low HDR of 0.144 45. Therefore, the linear time domain response of only the excited frequency (orange) also seems to visually capture the dominant characteristics of the measured signal. We also show a corresponding plot of the upper-outer D-alpha response as function of the applied ΔR_{sep} input in figure 5(*b*). In this figure, non-linear components will manifest as a deviation from the straight line which originates from the linear contribution. A phase shift of -13.092 degrees (or equivalently -0.455 ms) has been applied to remove the

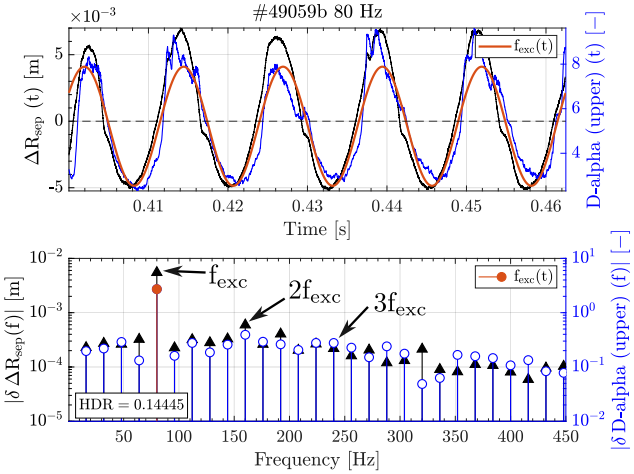

(a) Upper-outer divertor D-alpha response in time and frequency domain, #49059b

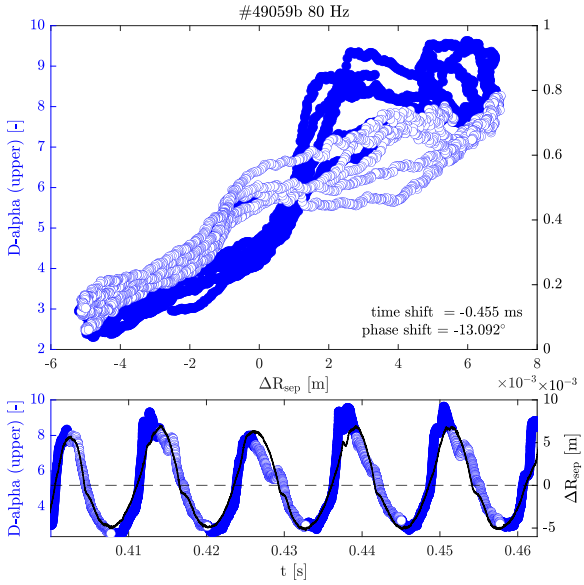

(b) Upper-outer divertor D-alpha response in time domain and as function of ΔR_{sep}, #49059b

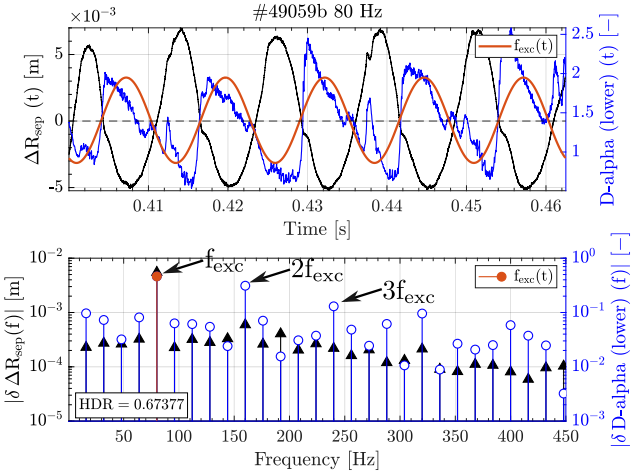

(c) Lower-outer divertor D-alpha response in time and frequency domain, #49059b

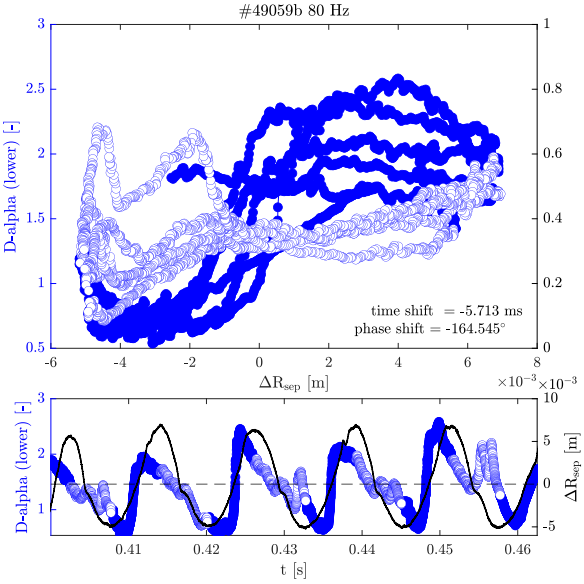

(d) Lower-outer divertor D-alpha response in time domain and as function of ΔR_{sep}, #49059b

Figure 5. Differences in linearity between upper-outer (*a*) and (*b*) and lower-outer divertors (*c*) and (*d*) with the latter indicating a significantly more non-linear D-alpha filterscope response. Figures (*a*) and (*c*) show the time domain (upper) and frequency domain (lower) response, including an overlay of the applied ΔR_{sep} input signal (black), the output response at the excited frequency (orange), and the harmonic distortion ratio (HDR). Figures (*b*) and (*d*) show the D-alpha response as function of ΔR_{sep} and in time domain with the indicated phase correction applied (or equivalent timeshift). The coloured and white dots indicate a positive and negative ΔR_{sep} movement respectively.

observed phase delay, extracted from the corresponding frequency response covered in section 4. Without such a correction, a fully linear system could be mischaracterised as a highly non-linear system as the response would resemble an ellipsoid. We observe that the response is mostly linear for $\Delta R_{sep} < 0$, traversing upwards (coloured dots) and downwards (white dots) in a similar manner. For $\Delta R_{sep} > 0$, we observe more scatter between the trajectories and the upwards (coloured dots) and downwards (white dots) traces seem to deviate. In time domain, this manifests as differences in the behaviour near the peaks of the applied sine wave. Nevertheless, a dominantly linear response seems to underpin the observed response across the whole ΔR_{sep} range with relatively minor differences between the upwards and downwards trajectories.

In contrast, we show the corresponding D-alpha filterscope response for the *lower-outer* divertor during the same shot in figure 5(*c*). We now observe a clear response above the noise floor for the harmonics of the excited frequency.

This indicates significant non-linear contributions in the signal, as evidenced by the relatively large HDR of 0.673 77. Consequently, the linear time domain response of only the excited frequency (orange) does not fully describe the signal. This is also illustrated in figure 5(*d*), clearly showing a major deviation from the linear trajectory with a large scatter between the trajectories. Furthermore, we observe major differences between the upwards (coloured dots) and downwards (white dots) trajectories.

Additionally, variations in the linearity of the divertor response was also observed between different experiments, for the same divertor and diagnostic. This is discussed in appendix G.

3.2. Discussion on linearity

The exact reason behind the occasionally observed non-linear behaviour remains presently unidentified. This is also contrary to the observation of dominantly linear divertor dynamics in experiments featuring gas fuelling and impurity seeding perturbations across devices [57], and MAST-U specifically [64]. However, the observed non-linear behaviour is not necessarily a result of the divertor power-sharing dynamics themselves as the upstream conditions also change in these scenarios. P_{sep} fluctuates through changes in NBI absorption efficiency and MHD activity, as discussed in section 2.1 and appendix A. From the perspective of the divertors, multiple (not necessarily periodic) perturbations are therefore applied simultaneously. This can best be investigated by repeating the experiments in H-mode scenarios with less MHD activity (which have since been developed). Alternatively, an ohmic L-mode scenario, which does not have this MHD activity, can be used to simultaneously also exclude any fluctuations from changes in beam absorption. In the remainder of this section, we discuss other possible, partial, explanations for the occasional non-linear behaviour.

Regardless of core effects, there is inherently a non-linear effect present in the power-sharing; for perturbations around a balanced configuration, small ΔR_{sep} perturbations have a relatively large influence on the power-sharing. However, for large ΔR_{sep} values, where the configuration starts to resemble a USN/LSN, the power is already dominantly carried by a single divertor set. In this situation, the change in power-sharing through an additional increase in ΔR_{sep} would be minimal. The effect of amplitude on the divertor response is discussed in detail in appendix G. We restrict our analysis to a comparable set of amplitudes to exclude this effect, as discussed in appendix H.

We have assumed an increase in D-alpha intensity to represent an increase in power flowing into the divertor as discussed in section 2. However, in addition to atomic contributions, D-alpha emission can also contain significant contributions from molecular processes at low temperatures ($T_{\mathrm{e}} < 2$ eV) [24, 65, 66]. It is therefore possible that the D-alpha intensity also increases when power is decreased, provided the sightlines capture the low temperature region, possibly contributing to the occasionally observed non-linear behaviour and scatter in the D-alpha measurements. In addition to this, although the D-alpha or D_2 Fulcher band emission might increase, its peak position might also vary and move beyond the diagnostic sight-cones. Therefore, although the total emission might increase, the D-alpha filterscopes or UFDS intensity measurements might register a decrease for some conditions (or vice-versa). Therefore, the diagnostic signals can be distorted compared to what would be expected from a pure intensity variation, contributing to the occasionally observed non-linear effects.

In our analysis, ΔR_{sep} is used as the input signal. However, ΔR_{sep} cannot be measured directly and follows from a combination of the EFIT++ reconstruction and the vertical control system signals, as discussed in section 2.2 and appendix D. It is therefore possible that the ΔR_{sep} used in our analysis is not fully correct. Therefore, the input perturbation applied to the system might have been different in reality, leading to errors in the extracted system response. For this reason, significant effort was invested into ensuring our ΔR_{sep} measurement is as accurate as possible with the measurements available, see appendix D.

3.3. Implications on power-sharing analysis

The principal aim of this work is to identify the power-sharing dynamics by comparing the divertor response across multiple frequencies. The main question is whether the power deposited at the divertor targets for a certain ΔR_{sep} amplitude decreases with frequency, regardless of the degree of non-linearity. The occasional observation of non-linear behaviour presents a complication, but does not prevent meaningful analysis. To better account for non-linear effects, we analyse the power ratio of the input and output signals—rather than the conventional magnitude response—as discussed in section 2.5. Additionally, we apply thresholds to restrict our dataset for analysis, this is discussed in appendix H.

4. Power-sharing dynamics

In this section, we investigate the power-sharing dynamics on MAST-U. We analyse the response of various diagnostics to the applied ΔR_{sep} perturbation in the frequency domain. We first discuss the outer divertor results followed by the inner divertor. Subsequently, we compare our *dynamic* results to *static* power-sharing scans. We end this section with a discussion.

4.1. Outer divertor response

The frequency response for the outer divertors is shown in figure 6. For all diagnostics, both the upper divertor (figure 6(*b*)) and lower divertor (figure 6(*c*)) response magnitude is approximately constant across all frequencies. This indicates that the perturbation magnitude registered by each diagnostic is irrespective of perturbation frequency. For example, consider the upper D-alpha response for a 40 Hz perturbation (#48648a, figure 6(*e*) and a 200 Hz perturbation (#49059a, figure 6(*f*). The experiments feature a similar ΔR_{sep} perturbation amplitude (4.7 mm, 4.6 mm respectively),

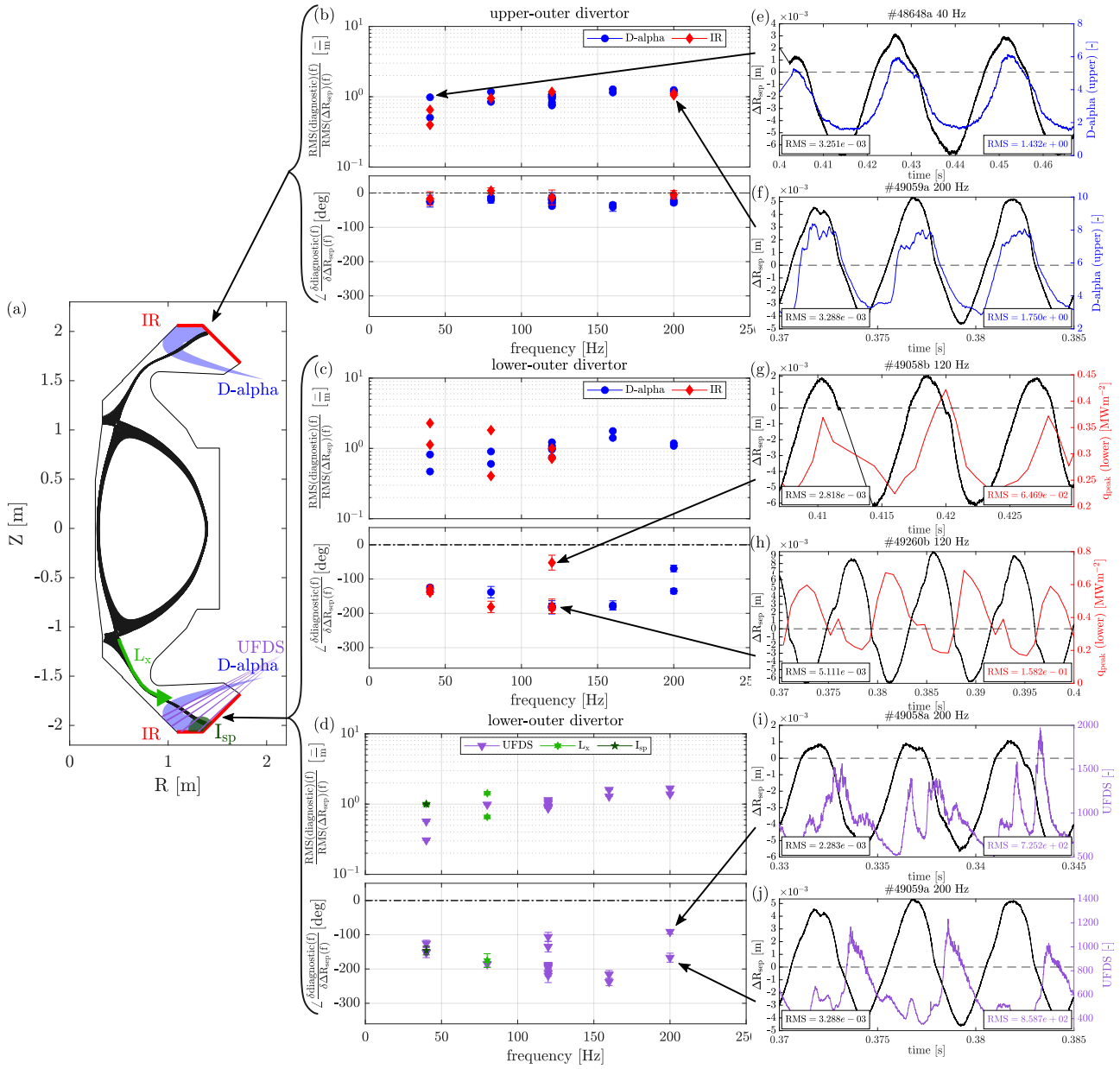

Figure 6. Outer divertor power sharing dynamics in frequency domain, showing no clear dependence on perturbation frequency (*a*) MAST-U poloidal cross-section showing the diagnostic field-of-views. (*b*)–(*d*) Upper-outer and lower-outer divertor bode plots. (*e*) and (*f*) Time domain zoom of D-alpha for 40 Hz and 200 Hz perturbations with comparable response. (*g*) and (*h*) Time domain zoom of IR illustrating phase scatter. Note that although the #49058b is downshifted while #49260b is balanced, the lowest ΔR_{sep} achieved is comparable. (*i*) and (*j*) Time domain zoom of UFDS illustrating phase scatter. Note that although the #49058a is downshifted while #49059a is balanced, the lowest ΔR_{sep} achieved is comparable.

and we also observe a similar 1.432 RMS and 1.750 RMS output response, despite the major difference in perturbation frequency.

Practically, this implies that the power-sharing reacts as strongly to slow perturbations as it does to faster perturbations. We see this conclusion supported by time domain measurements in figures 7 and 8. We first consider figure 7 which shows the incident heat flux q_{peak} on the upper-outer divertor, for two different perturbations applied sequentially during the same shot. The perturbations have a comparable amplitude, but differ greatly in perturbation frequency: $f = 200$ Hz for #49059a, and $f = 80$ Hz for #49059b. Despite the perturbation frequency difference, q_{peak} is comparable at $0.6 - 0.8\,\mathrm{MWm}^{-2}$ for both perturbations. This is in agreement with the observation that the gain of the system is not reduced for higher perturbation frequencies. We now consider figure 8 which shows the inverted Fulcher band emission front response to a 200 Hz perturbation in #49059a. The front position is shown in the centre panel while the surrounding panels are all successive camera images. The detected front position L_x is indicated with a green arrow, tracked along the separatrix provided by EFIT++ which is shown in grey. The

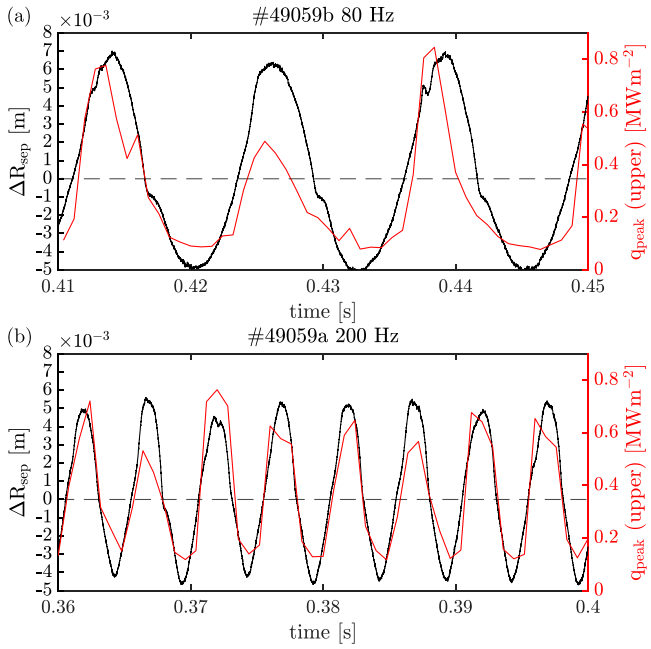

Figure 7. Peak incident heat flux q_{peak} in the upper-outer divertor for a similar ΔR_{sep} amplitude, showing a comparable response for high and low frequencies. (*a*) $f_{\text{exc}} = 80$ Hz. (*b*) $f_{\text{exc}} = 200$ Hz. Note that the perturbations have been applied sequentially, within the same experiment.

frames shown are 2.5 ms apart, which corresponds to half a perturbation period. The images show that within this time span, the ionisation front changes from deeply detached to fully attached. The time domain panel shows that this can be observed consistently throughout the perturbation. This implies that the plasma detaches and fully re-attaches, despite the 200 Hz perturbation frequency.

The frequency response in figure 6 also indicates a clear difference in the upper-outer and lower-outer divertor phase delay. This originates from the sign difference between the upper-outer and lower-outer divertors: an increase in ΔR_{sep} transitions the system towards an upper single null configuration, leading to an increase in power flowing towards the upper-outer divertor and a corresponding decrease in power flowing towards the lower-outer divertor. This manifests as a 180 degree phase difference in figure 6.

It can also be observed that the phase response for the lower-outer divertor (figures 6(*c*) and (*d*)) appears to have a much larger spread compared to the upper-outer divertor (figure 6(*b*)), consistent with the observation of a cleaner, more linear response for the upper-outer divertor in section 3. For example, consider the IR response for #49058b and #49260b in figures 6(*g*) and (*h*), respectively. Both shots use a 120 Hz perturbation frequency, but show significantly different phase behaviour (60 and 180 degrees, respectively). This can even be observed by eye in the time domain plots: the response peak in figure 6(*g*) is consistently located closer to the corresponding perturbation peak compared to figure 6(*h*). The same effect can be observed for the UFDS response for a 200 Hz perturbation for #49058a and #49059a in figures 6(*i*) and (*j*), respectively.

As noted in section 3.2, the exact cause for the occasionally significant differences between shots is presently unclear, but might be related to changes in core conditions.

4.2. Inner divertor response

The frequency response for the inner divertors is shown in figure 9, painting a similar picture to the outer divertors discussed in section 4.1. The response magnitude for the lower-inner divertor (figure 9(*c*)) is approximately constant across all frequencies. This indicates that the perturbation magnitude registered by each diagnostic is irrespective of perturbation frequency. For example, consider the upper inner RBA response for a 40 Hz perturbation (#48648a, figure 9(*f*) and 200 Hz perturbation (#49059a, figure 9(*g*). The experiments feature a similar ΔR_{sep} perturbation amplitude (4.7 mm, 4.6 mm respectively), and we also observe a similar 0.1090 RMS and 0.1297 RMS output response, despite the major difference in perturbation frequency.

This, similarly to the outer divertors, implies that the power-sharing reacts as strongly to both faster and slower perturbations. A time domain analyses supports this conclusion in figure 10 where we show XPI inversions of the lower-inner divertor for the 200 Hz perturbation in #49059a. Note that this is the same shot as discussed for the outer divertor in figure 8. In figure 10, the centre panel shows the lower-inner divertor D_2 Fulcher strikepoint intensity I_{ISP}. The surrounding frames show the corresponding Fulcher band camera inversions, which are 2.5 ms apart, corresponding to half a perturbation period. We also show the HSV D-alpha images for these timestamps, the corresponding time trace is shown in figure 9(*g*). Contrary to the lower-outer divertor shown in figure 8, the D_2 Fulcher-band filtered images in figure 10 show that the ionisation front remains attached throughout the perturbation. However, the time domain evolution of I_{ISP} shows that the strikepoint intensity does vary noticeably. The HSV D-alpha response is clearly observable in the camera image, and is even clearer in the corresponding time trace in figure 9(*g*). The divertor therefore clearly responds to the applied 200 Hz perturbation, as concluded for the lower-outer divertor in figure 8, although remaining attached throughout the perturbation.

Compared to the outer divertors in figure 6, there is considerably more scatter in the inner divertor frequency response in figure 9. This is especially the case for the upper-inner divertor (figure 9(*b*)) where the only available diagnostic is the HSV. As discussed in appendix F, this diagnostic is especially sensitive to the exact placement of the region of interest (ROI) near the strikepoint and an unknown effect appears to attenuate the upper divertor response. This effect is most pronounced for downshifted perturbations, perhaps as these configurations direct relatively little power towards the upper divertor. As most of the lower frequency experiments used downshifted equilibria, there are no frequency datapoints available below 120 Hz. Furthermore, we observe a significant scatter in both the magnitude and phase response. Comparing the 120 Hz perturbations #49260c (figure 9(*d*)) and #48648a (figure 9(*e*)), we

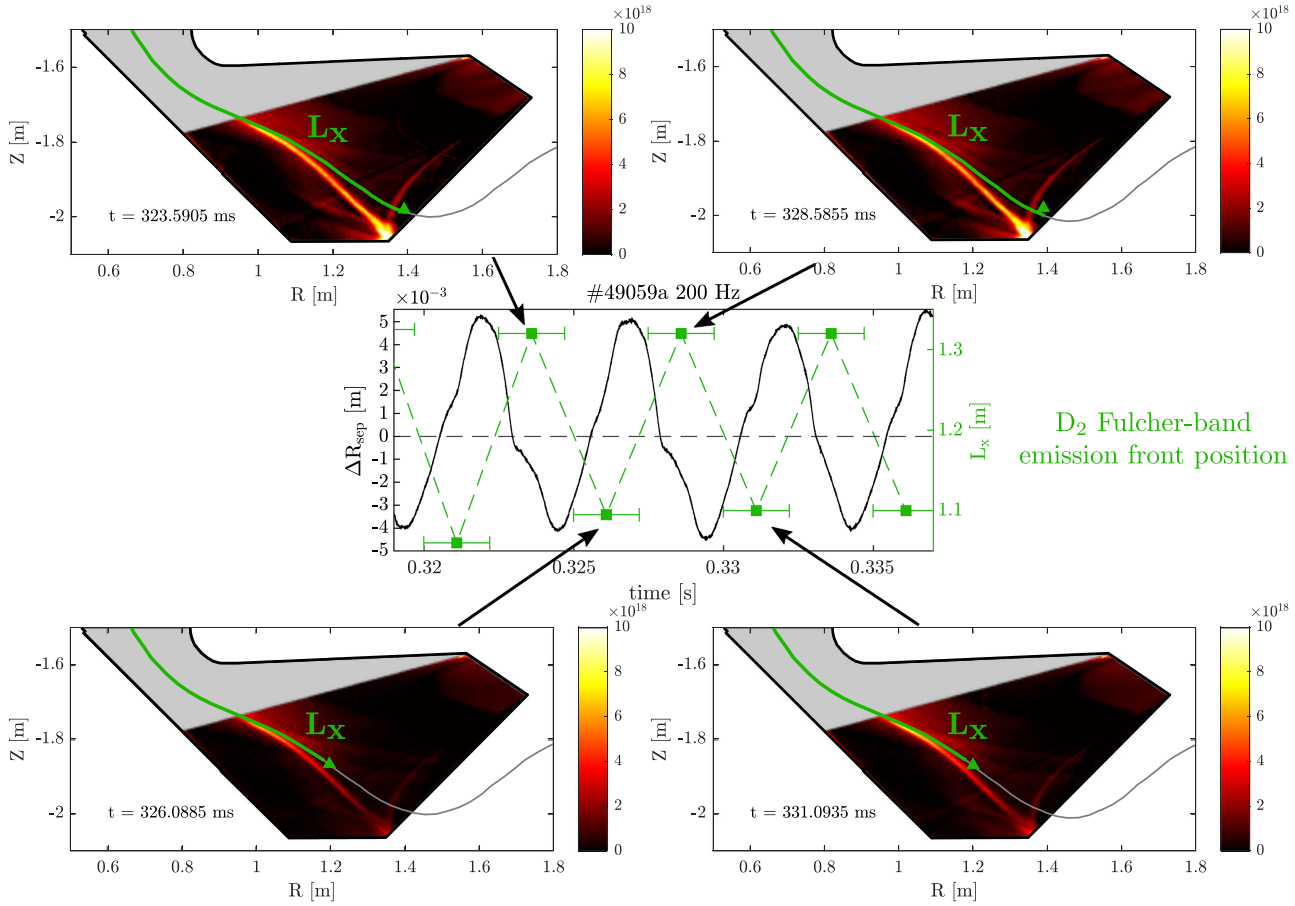

Figure 8. Lower-outer divertor D_2 Fulcher band emission front response to a 200 Hz ΔR_{sep} perturbation, showing a transition from fully attached to deeply detached within the frame resolution of the MWI camera system. The centre figure shows the applied ΔR_{sep} perturbation and the poloidal distance from the detected front position to the X-point L_x, with the errorbars indicating the camera exposure time of ≈ 2.5 ms. The surrounding figures show inverted MWI Fulcher band camera images, with the detected L_x overlayed in green and the separatrix according to EFIT++ shown in grey.

observe a major difference in phase delay. Note that while #48909a is downshifted and #49260c is balanced, the lowest $A_{\max,\Delta R_{sep}}$ achieved is comparable. The limited datapoints, combined with the observed scatter, deem the upper-inner divertor frequency scan to be inconclusive.

We do note that for the lower-inner divertor in figure 9(*c*), the phase delay seems to decrease with perturbation frequency. The cause of this behaviour is presently unclear, however, the HSV has a 1 kHz acquisition frequency (see table 2). For a 200 Hz perturbation frequency, this implies that there are only 5 datapoints available per period, while for a 40 Hz perturbation, 25 datapoints are available per frequency. Although the timing in the presented data has already been corrected as discussed in appendix C, these datapoints are very close to the $f_{diag}/f_{exc} > 4$ threshold set in appendix H and are consequently sensitive to otherwise minor timing discrepancies and noise.

4.3. Comparison to static power-sharing

A commonly used, power-sharing model available in literature is the Brunner model [28]. This is a *static* model, it does not consider any dynamic effects. It has been shown to agree with static experiments on Alcator C-Mod [28], DIII-D [38], MAST [39, 40], EAST [42], and TCV [29]. It consists of a logistic function for the upper-to-lower power-sharing, parametrised by the inner and outer heat flux SOL e-folding width λ_i and λ_0. This is combined with a Gaussian function to describe the inner-to-outer power sharing with λ_{io} as the characteristic Gaussian width. The Brunner model implies that for large absolute values of ΔR_{sep}, the discharge becomes fully LSN or USN and, secondly, the inner heat load is decreased strongest for ΔR_{sep} values close to zero. For more details, refer to [28]. We select the values shown in table 3 in our evaluation of the Brunner model for MAST-U (see figure G3 for the resulting power-sharing diagram). Not all model parameters have been measured for MAST-U, therefore, some are obtained by rescaling literature data [28], which introduces considerable uncertainty.

The dynamic power-sharing results are compared to quasi-static experiments and the Brunner model in figure 11. The upper-outer D-alpha response as function ΔR_{sep} is shown in figure 11(*a*) for a balanced 200 Hz perturbation in #49059a, a slow ramp towards a LSN in #49220, and a slow ramp towards an USN in #49262. The corresponding

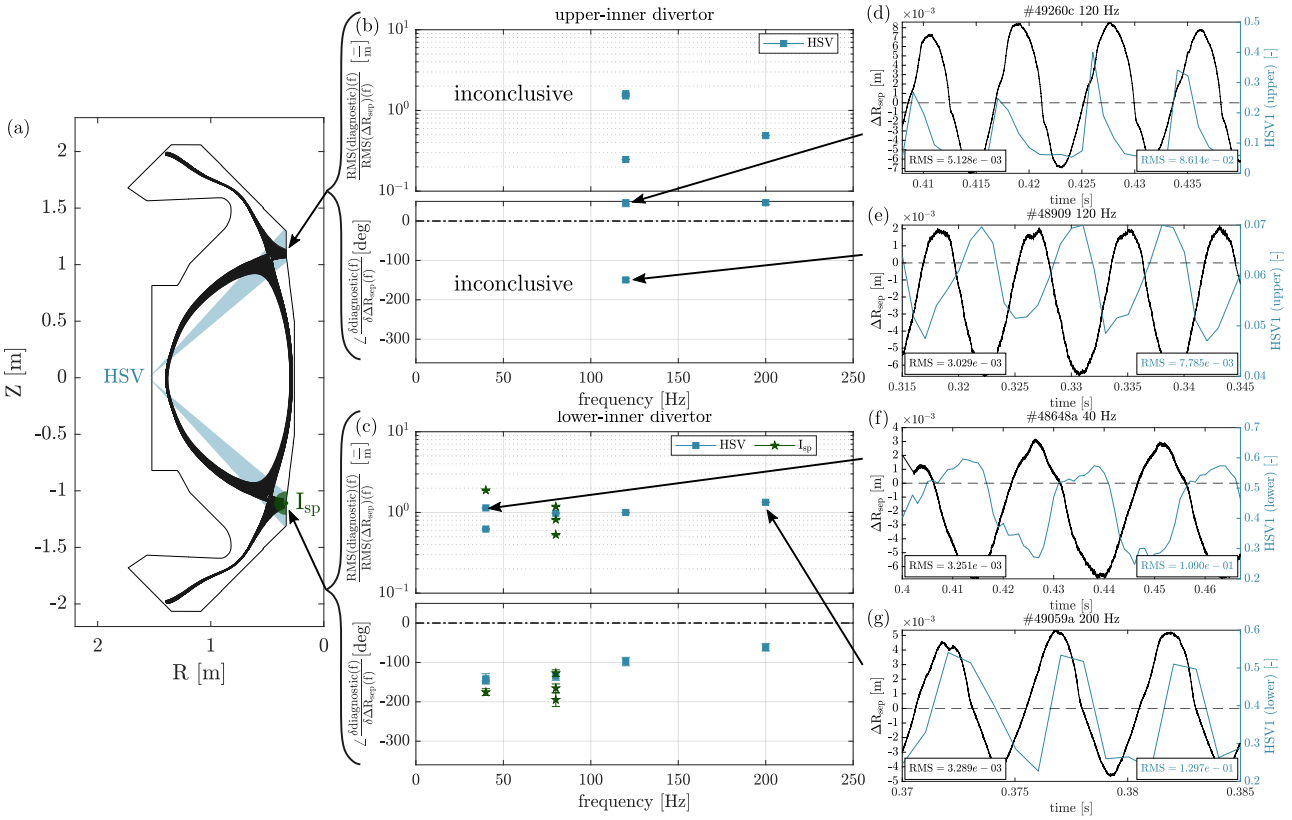

Figure 9. Inner divertor power-sharing dynamics in frequency domain, showing no clear dependence on perturbation frequency. (*a*) MAST-U poloidal cross-section showing the diagnostic field-of-views. (*b*) Inconclusive upper-inner divertor bode plot. (*c*) Lower-inner divertor bode plot. (*d*) and (*e*) time domain zoom of HSV1 illustrating a major difference in phase delay. Note that while #48909a is downshifted and #49260c is balanced, the lowest ΔR_{sep} achieved is comparable (*f*) and (*g*) Time domain zoom of HSV1, showing a comparable magnitude but a shift in phase response.

time domain representations are shown in figures 11(*b*)–(*d*). Note that it is unclear how the power fraction quantitatively relates to the employed D-alpha measurement, therefore, the power fraction is plotted on a different *y*-axis. The exact slope between the Brunner model and the D-alpha response should therefore not be compared directly. As discussed in section 3.1, we remove the phase delay from the dynamic perturbation experiment to prevent any influence on figure 11(*a*).

In figure 11(*a*), we observe a dominantly linearly response within the probed ΔR_{sep} range. The slope is comparable between the slow ramps (#49220, #49262) and the dynamic experiment (#49059a). This implies that there is no inherent difference in power sharing between the slow ramps and the fast 200 Hz perturbation experiment, in line with our observations from section 4 that the power-sharing reacts as strongly to slow perturbations as it does to faster perturbations. The linear power-sharing curve predicted by the Brunner model seems to resemble the measured linear D_{alpha} response for both ramps and the dynamic perturbation experiment. Consequently, the static Brunner power-sharing model also appears suitable to describe the power-sharing trend for perturbations up to (at least) 200 Hz in MAST-U.

5. Discussion

In this discussion section, we first discuss our results on power-sharing dynamics, followed by the implications for power reactors.

5.1. Power-sharing dynamics

In our experiments, we have characterised the power-sharing dynamics in MAST-U. The results indicate that the divertor response to DN power-sharing fluctuations is approximately constant across the probed 40–200 Hz frequency range, i.e. the divertor reacts as strongly to slow perturbations as it does to faster perturbations. As explored in section 4.3, the divertor response during fast power-sharing perturbations closely matches the response during slow ramps. Consequently, the static Brunner power-sharing model is well-suited to also describe the power-sharing for fast perturbations.

Occasionally, significant differences in divertor response for upwards and downwards ΔR_{sep} movement have been observed (figures 5(*d*) and G1(*d*)). In contrast, other cases traverse largely along the same trajectory in both directions (figures 5(*b*) G1(*b*), and G2). It is important to note that this

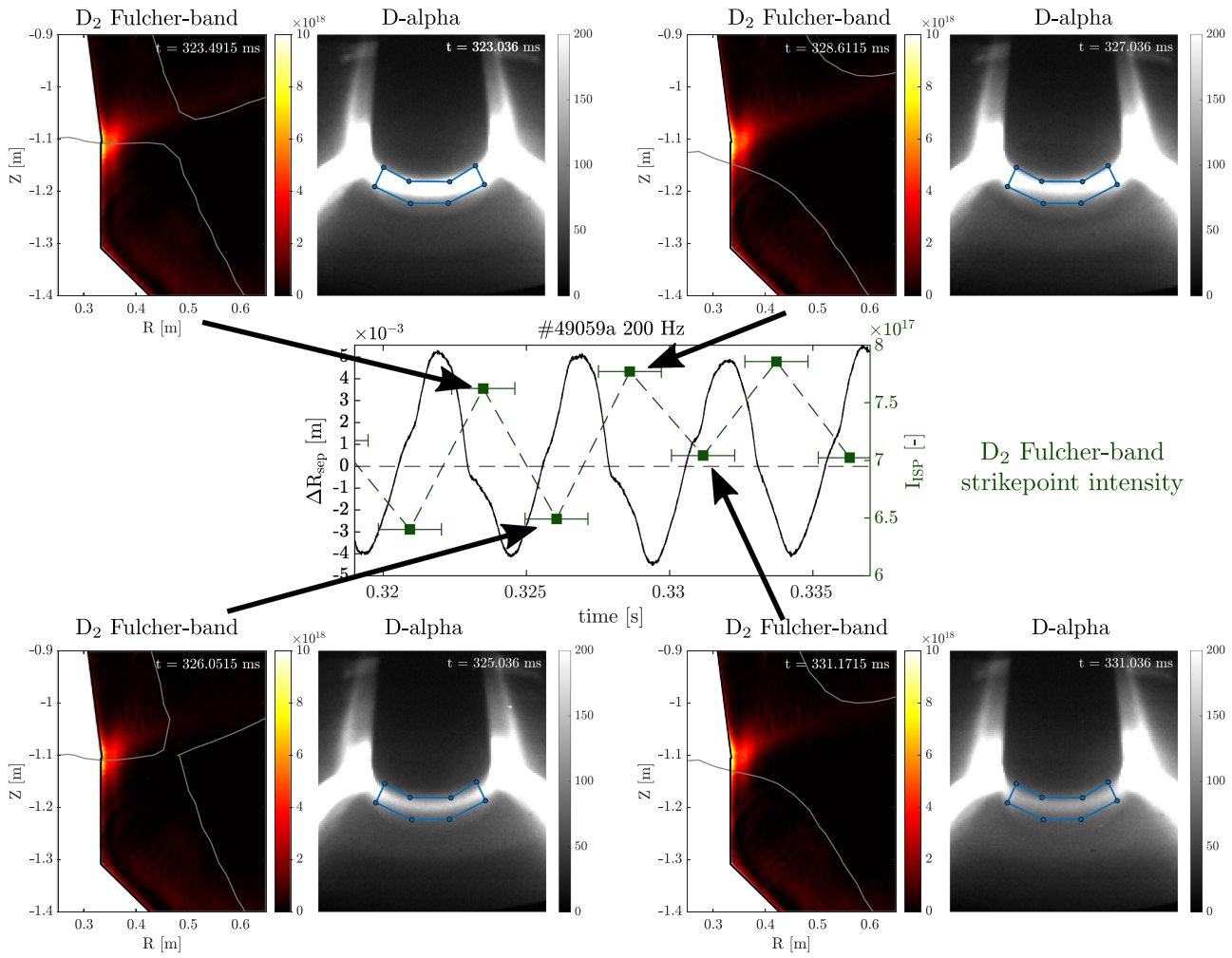

Figure 10. Lower-inner target response to a 200 Hz ΔR_{sep} perturbation, showing a response in D-alpha and D_2 Fulcher-band intensity while remaining attached throughout the perturbations. The centre figure shows the applied ΔR_{sep} perturbation and the D_2 Fulcher-band strikepoint intensity from XPI camera inversions, with the errorbars indicating the ≈ 2.5 ms camera exposure time. The surrounding figures shown inverted XPI D_2 Fulcher-band images and the corresponding HSV D-alpha images, with the region-of-interest used for the intensity calculation shown in blue and the separatrix according to EFIT++ shown in grey. Note that corresponding HSV D-alpha intensity time evolution is shown in figure 9(*g*).

Table 3. Parameters for the Brunner model [28] used in figures G3 and 11(*a*).

Param	Value	Meaning
$f_{\mathrm{i},0}$	0.2[a]	Inner power fraction at $\Delta R_{\mathrm{sep}} = 0$
$f_{\mathrm{i},\infty}$	0.25[b]	Inner power fraction at $\Delta R_{\mathrm{sep}} \to \pm\infty$
λ_{io}	30.8 mm[c]	Gaussian inner-to-outer width
λ_{i}	13.9 mm[d]	Inner e-folding width
λ_{o}	7.85 mm[e]	Outer e-folding width

[a] Measured using IR in #49404, using Lower-Single-Null, H-mode, Conventional Divertor, $I_{\mathrm{p}} = 750$ kA scenario.
[b] Measured using IR in #49213, using Lower-Single-Null, H-mode, Conventional Divertor, $I_{\mathrm{p}} = 750$ kA scenario.
[c] Rescaled from $\lambda_{\mathrm{io}} = 1.57$ mm and $\lambda_{\mathrm{o}} = 0.40$ mm in [28], by taking the ratio to the measured $\lambda_{\mathrm{o}} = 7.85$ mm.
[d] Rescaled from $\lambda_{\mathrm{i}} = 0.71$ mm and $\lambda_{\mathrm{o}} = 0.40$ mm in [28], by taking the ratio to the measured $\lambda_{\mathrm{o}} = 7.85$ mm.
[e] Measured in Double-Null, H-mode, Conventional Divertor, $I_{\mathrm{p}} = 750$ kA scenario [67].

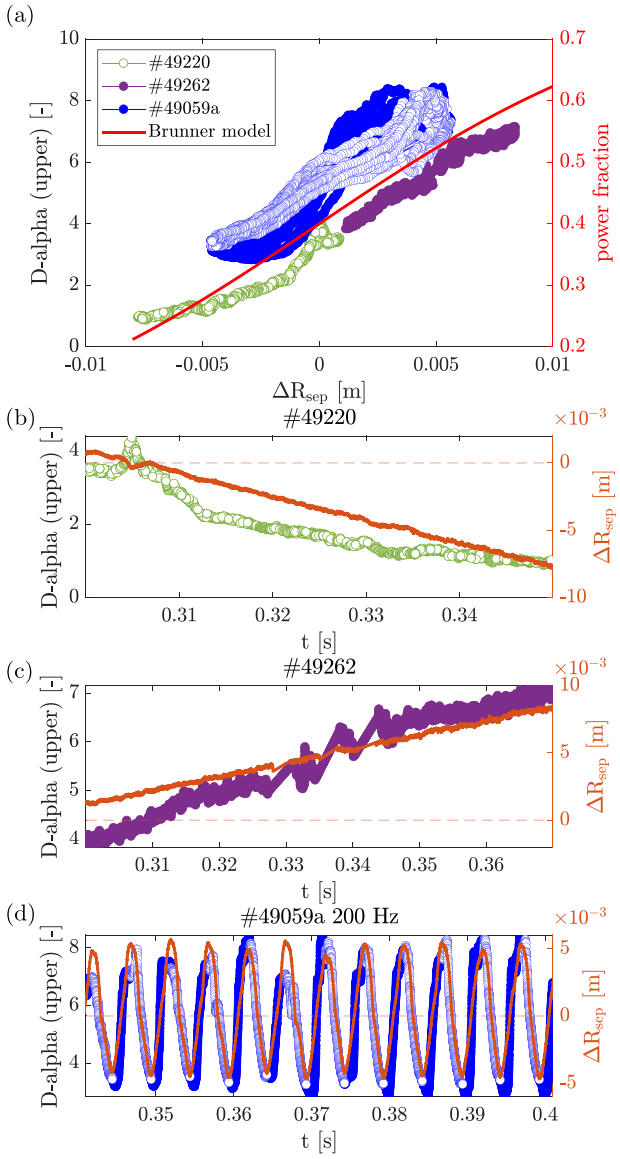

Figure 11. Comparison of the upper-outer D-alpha response to quasi-static ramps and dynamic 200 Hz perturbations, showing a comparable response and alignment with the static Brunner model [28]. (*a*) Upper-outer divertor D-alpha response as function of ΔR_{sep} for a slow ramp towards LSN #49220, a slow ramp towards USN #49262, and a 200 Hz sinusoidal perturbation around a connected DN #49059a. The coloured and white dots indicate a positive and negative ΔR_{sep} movement respectively. The Brunner model [28] is overlayed in red, utilising the parameters displayed in table 3. (*b*)–(*d*) Time domain response and the applied ΔR_{sep} perturbation for #49220, #49262, and #49059a the latter employing a phase shift of −28.478 degrees (equivalent to −0.396 ms) to remove any phase delay, as discussed in section 3.1.

asymmetry is separate from the occasionally observed non-linear behaviour in section 3.2, as a non-linear system can still follow the same path both during upwards and downwards perturbations. The degree to which we see this asymmetry varies considerably across shots and diagnostics. This behaviour is not predicted by the Brunner model, and is absent in the ramp experiments, see figure 11. However, the ramp experiments only feature uni-directional movement–either downwards or upwards. Hence, the trajectory asymmetries occasionally observed in the dynamic shots might also be present for slow ramps but remain unexplored within the current data set. The underlying mechanism behind this effect has not yet been identified. However, it might also be related to the variations in core conditions discussed in section 3.2. Further experiments featuring slow ramps, employing both increasing and decreasing ΔR_{sep} within each experiment, would allow the occasionally observed asymmetric behaviour to be ascribed to a static or dynamic effect.

Additionally, as discussed in section 2.4, the divertor leg position has been observed to vary as a result of the vertical position perturbation. The effect is relatively minor according to the EFIT++ magnetic reconstruction, with the leg remaining in view of all diagnostics. However, significant deviations between EFIT++ and the actual divertor leg position can occur in these experiments. This is illustrated in figure 8, where there is a significant deviation between the EFIT++ reconstruction and optical position of the divertor leg according to the D_2 Fulcher emission. It is possible that divertor leg movement is more severe than captured by EFIT++ and might still have affected the results by varying how much of the radiative region around the divertor leg is observed by the sightcones of each diagnostic during the perturbation, leading to an asymmetric response.

In sections 4.1 and 4.2, a significant spread has been observed in the magnitude and especially phase response for the lower-outer divertor and upper-inner divertors. This spread can also be observed in the raw time domain plots (see figures 6(*e*)–(*j*) and 9(*d*), (*e*)), suggesting a physical origin, though some influence from signal processing or diagnostic geometry cannot be fully excluded. The reason for this spread is unclear, it is however striking that the down-shifted perturbations appear to consistently show a decreased phase delay w.r.t. the balanced configurations, see appendix I. The observed spread across experiments might be related to the changes in core conditions discussed in section 3. To investigate this further, additional experiments could be conducted in scenarios without MHD activity, employing either H-mode or L-mode. Ohmically-heated scenarios can be employed to diagnose to which degree the changes in NBI-plasma coupling affects the observed response.

Bifurcation-like behaviour [68], driven by a condensation-(impurity) radiation instability, may occur in DN divertors according to theoretical work, resulting in one attached and one detached divertor. This would imply that simultaneous detachment of both upper and lower divertors is difficult to sustain, which is consequently seen as a potential concern for DN based power exhaust solutions in reactors [69]. Strong decoupling between the lower and upper outer

divertors is observed in the (detached) MAST-U DN Super-X divertor. Both divertors are simultaneously detached [24, 70] and adding moderate amounts of additional fuelling in one divertor changes its detached state without impacting the other divertor—which should enable independent control of both divertors [64]. Even in our dynamic double null experiments, where we purposefully apply power-sharing perturbations (up to 200 Hz), we observe smooth transitions (subject to experimental constraints) from a balanced configuration towards LSN or USN by adjusting ΔR_{sep} (see figures 11 and G2(a)). Although these results may alleviate some of the concerns of DN divertors, further research is required during extrinsic impurity injection (although intrinsic carbon impurities are present which radiate significantly upstream of the baffle [66]) and in X-point radiator regimes.

The results presented in this paper are exclusively based on MAST-U experiments. Additional dynamic power-sharing experiments in other devices could provide valuable insight into the mechanisms behind our observations.

5.2. Implications for power reactors

Our work highlights the power-sharing challenges in DN fusion power reactors, arising from their demanding vertical control requirements. Our results indicate that no significant reduction in power reaching the divertor targets is to be expected through power-sharing dynamics, at least within the considered 200 Hz frequency range. While such dynamics may still exist at higher frequencies, the chosen maximum frequency of 200 Hz likely already surpasses the feasible oscillation frequency for reactor-scale devices [4]. It therefore seems unlikely that such devices can reduce the power reaching the divertor target through dynamical power-sharing effects, assuming that our observations are transferable to reactor-scale devices.

The analysis presented in this work only considers the plasma dynamics. Although our work concludes that power-sharing perturbations directly arrive at the divertor targets, the thermal conductivity of the divertor tile material also plays a role. For sufficiently fast perturbations, the finite conductivity will dampen the bulk temperature response of the material. Purposefully applying power-sharing perturbations (i.e. a dynamic-double null scenario) might therefore result in a reduction of bulk divertor tile temperatures. This still exposes the surface of the divertor tiles to cyclic loads. Such cyclic loading has been found to significantly promote divertor tile cracking [71, 72], and therefore poses a serious engineering concern.

Magnetic control strategies should prioritise maintaining the most balanced power-sharing configuration possible. Some degree of power-sharing oscillations are likely unavoidable in DN power reactors. Handling such rapid fluctuations can exceed the response time of relatively slow gas actuators employed for exhaust control [57, 64]. Therefore, ADCs that offer enhanced passive transient handling capabilities present an attractive proposition [64, 70].

6. Conclusions

We present the first dynamical analysis of divertor power-sharing in DN tokamaks. We have employed a frequency domain approach to study the power-sharing dynamics in MAST-U as a result of ΔR_{sep} perturbations ranging from 40–200 Hz with various amplitudes. We conclude that the outer and inner divertor power-sharing dynamics do not indicate any significant dynamics effects: both the gain and phase response is approximately constant over frequency. This implies that dynamic power-sharing perturbations up to 200 Hz produce divertor target loads comparable to those observed in a static scenario with the same magnetic imbalance. Although dynamic effects might still exist at higher frequencies, our results show that static power-sharing models are also suitable to describe a dynamic situation up to 200 Hz.

The divertor response to the applied perturbations was predominantly linear in most of our experiments, however, some experiments exhibited a notable non-linear response. Additionally, a significant scatter was observed between our measurements. The underlying cause of this behaviour remains unclear, though we suspect the variations core plasma conditions to be the primary contribution, instigated through MHD activity and changes in NBI-plasma coupling. Asymmetries between positive and negative ΔR_{sep} trajectories were also occasionally observed, likely related to these core effects, though the exact mechanism remains unknown.

Acknowledgments

The authors would like to thank J Veenendaal and M Lauret for their contributions in discussions considering the data analysis. This work has been carried out within the framework of the EUROfusion Consortium, funded by the European Union via the Euratom Research and Training Programme (Grant Agreement No. 101052200 - EUROfusion). Views and opinions expressed are however those of the author(s) only and do not necessarily reflect those of the European Union or the European Commission. Neither the European Union not the European Commission can be held responsible for them. This work has been part-funded by the EPSRC Energy Programme (Grant Number EP/W006839/1). This work was supported by the U.S. Department of Energy under Grant No. DE-AC05-00OR22725.

Appendix A. Core plasma fluctuations

In this appendix, we discuss the observed fluctuations in core conditions during our experiments.

The H-mode scenario employed in this work suffers from strong MHD activity. This is illustrated by the spectrograms in figures A1(a) and A2(a). In all experiments, we observe high frequent (>50 kHz) MHD activity, starting around 200 ms.

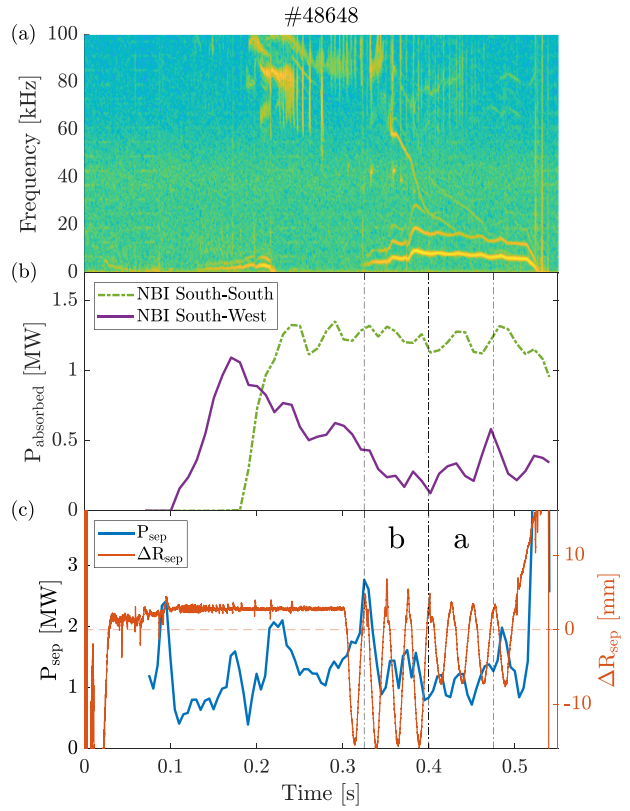

Figure A1. Core plasma conditions for downshifted 40 Hz perturbation #48648. (*a*) MHD spectrogram, showing both higher frequency ($>$ 50 kHz) and lower frequency ($<$ 50 kHz) activity. (*b*) Core plasma absorbed beam power P_{absorbed} for the South–South and South–West NBI systems, inferred from TRANSP [73] (*c*) Applied ΔR_{sep} perturbation and separatrix power P_{sep} inferred from TRANSP [73]. The subdivision into perturbation sections according to table 1 is indicated by the letters a and b.

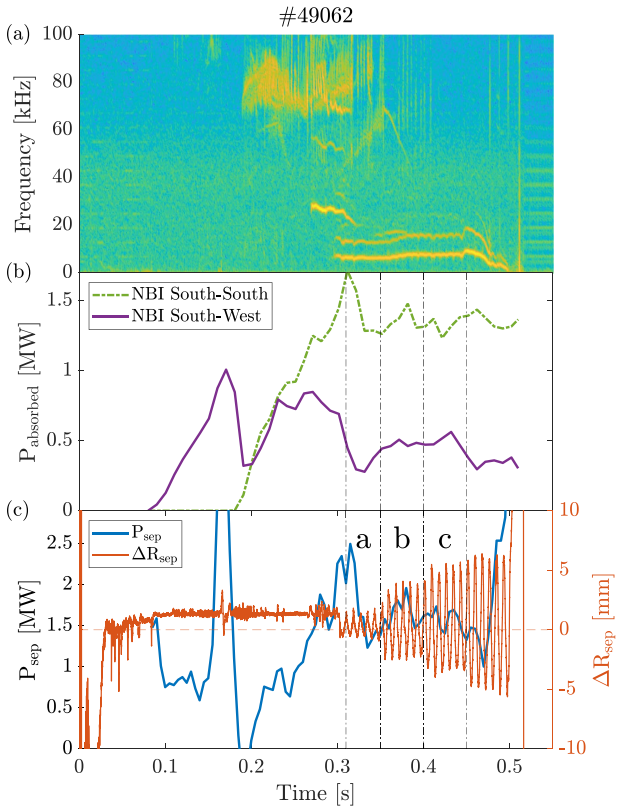

Figure A2. Core plasma conditions for balanced 120 Hz perturbation #49062. (*a*) MHD spectrogram, showing both higher frequency ($>$ 50 kHz) and lower frequency ($<$ 50 kHz) activity. (*b*) Core plasma absorbed beam power P_{absorbed} for the South–South and South–West NBI systems, inferred from TRANSP [73] (*c*) applied ΔR_{sep} perturbation and separatrix power P_{sep} inferred from TRANSP [73]. The subdivision into perturbation sections according to table 1 is indicated by the letters a, b, and c.

Lower frequency activity ($<$ 50 kHz) appears around 250–350 ms. This is perhaps (partially) a result of the applied vertical position oscillations to achieve the ΔR_{sep} perturbations (shown in orange in figures A1(*b*) and A2(*b*). As a result, the core plasma conditions vary considerably throughout each shot. Each shot ends through a disruption trigged by MHD mode-locking.

In addition to this, the scenario is fuelled through both on-axis and off-axis NBI fuelling, both at 1.5 MW. As discussed in section 2.1, the applied vertical oscillations likely also affect the beam fuelling efficiency as the beam intersects more or less of the plasma core depending on its vertical position. This leads to fluctuations in the power deposited into the core plasma, as can be observed in figures A1(*b*) and A2(*b*). The traces shown are inferred from TRANSP [73]. Here, we see that the absorbed power for both NBI systems fluctuates significantly as a result of the applied perturbations.

The MHD activity combined with the variations in beam absorption culminates in a, not necessarily periodic, change in separatrix power P_{sep} as shown in the figures A1(*c*) and A2(*c*). The shown P_{sep} traces are extracted from TRANSP simulations [73]. The fluctuations in absorbed power in #48648 (figure A1) are on the order of 0.1–0.2 MW for each NBI system, contributing significantly the observed 0.2–0.5 MW P_{sep} fluctuations. It is likely the variations in P_{sep} have affected the results shown in this paper, being a prime suspect for the occasionally observed non-linear behaviour (section 3.2) and the large scatter between experiments (section 5).

Appendix B. Diagnostics

In this appendix, we provide more detail on the various diagnostics considered in this work. The sight-cones of each diagnostic are shown in figure B1 and their divertor target coverage is listed in table 2. Their acquisition frequencies are also shown in table 2.

B.1. D-alpha filterscopes

These photo-multipier tubes provide a line-integrated measurement of the deuterium Balmer-alpha emission intensity which arises as a result of various atomic and molecular

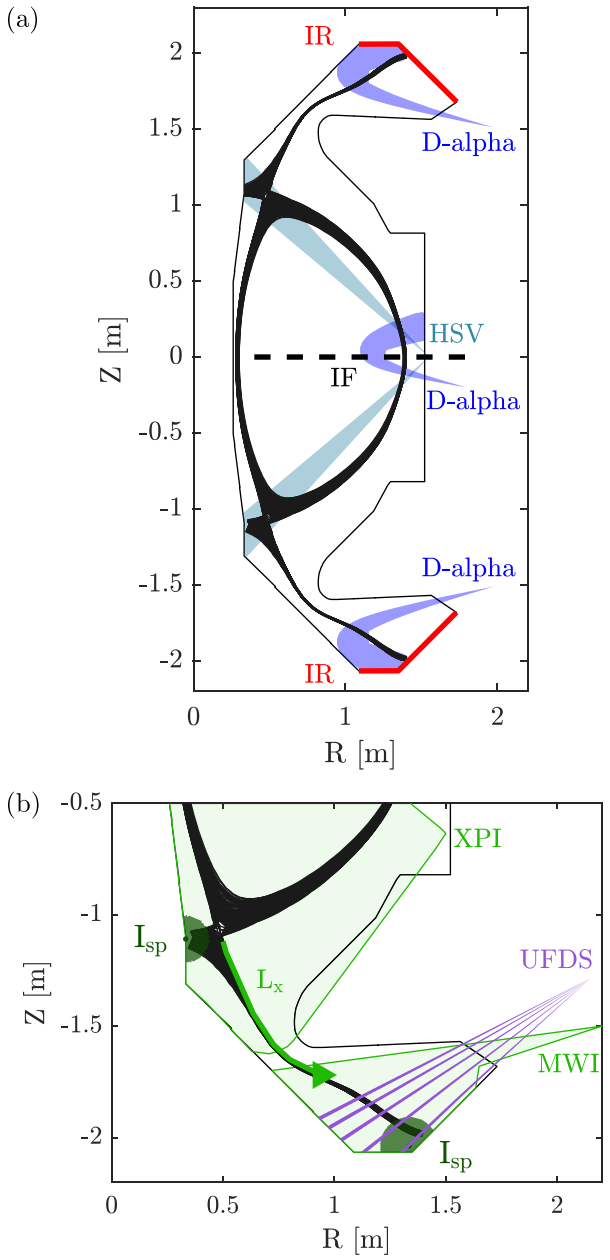

Figure B1. Overview of the MAST-U diagnostics used in this study. The separatrix range of movement according to the EFIT++ magnetic reconstruction in #49062 is shown in black. (*a*) Approximate sight-cones of the HSV camera D-alpha intensity measurement, core IF, lower divertor D-alpha, midplane D-alpha, upper divertor D-alpha, and the target area covered by the upper and lower IR cameras. (*b*) Lower part of the vessel, indicating the approximate sight-cones of the UFDS system and the XPI and MWI spectral imaging systems. The regions of interest for the strike point intensity I_{sp} for the spectral imaging systems are shown in dark green. The front position length L_x w.r.t. the lower X-point is indicated by the green arrow.

reactions [24, 58, 65], indicating plasma-neutral interaction. The neutral pressure is not expected to evolve on timescales resembling the applied perturbations (⩾40 Hz). Therefore, for a constant neutral pressure, observed fluctuations in D-alpha intensity mostly indicate electron temperature and/or density fluctuations. These, we assume, are driven by fluctuations in the power reaching the divertor. We employ the HL02-B tangential and HU10-B tangential filterscopes for the lower-outer and upper-outer divertors respectively. Also, we used the HM10-E tangential filterscope located near the midplane to detect the occurrence of ELMs in the plasma core. All scopes have been operated at 100 kHz for all shots.

B.2. Spectral imaging (XPI, MWI)

MAST-U features spectral imaging cameras focussed on the lower divertor (MWI) and lower X-point (XPI). These systems provide 2D emission intensity images for various spectral lines [65, 74, 75]. In this study, we track the D_2 Fulcher-band emission location as a proxy for the ionisation region [24, 58, 59]. The obtained images are poloidally inverted to extract the trailing edge of the emission front position in the lower-outer divertor [65], expressed as the distance from the D_2 Fulcher front to the lower X-point (L_x). This is a proven, direct measurement of the detachment state of the plasma [24, 59, 65], in this case increasing when the plasma becomes more attached. We also extract the emission intensity around each lower strikepoint as I_{sp}. Both camera systems run at a 400 Hz acquisition frequency.

B.3. High-speed video (HSV)

We employ a High-Speed Visible light camera, the HSV1, located at the midplane. It is equipped with a D-alpha spectral filter, the resulting image is therefore indicative of plasma-neutral interaction similarly to the D-alpha filterscope results. The core plasma is prominently in view, as can be observed in figure B1. However, as plasma-neutral interaction occurs predominantly near the edge of the plasma and in the divertor chambers, the core is mostly transparent in these images such that the inner strikepoints can be observed. We take the average of the pixel intensity around each respective target to generate signals for the upper-inner and lower-inner divertors, see appendix F. Similarly to the D-alpha filterscopes, we interpret these signals as indicative of the power arriving at the upper-inner and lower-inner targets. The HSV camera system is operated at 1 kHz.

B.4. Ultra-fast divertor spectroscopy (UFDS)

The UFDS diagnostic is available in the lower-outer divertor. This system measures the line-integrated intensity for Balmer-alpha, Balmer-beta, and D_2 Fulcher-band. We use the D_2 Fulcher intensity as a proxy for ionisation, similar to the spectral imaging strikepoint intensity (I_{sp}), taking the average over the five sight-cones located in the lower divertor. The UFDS system is operated at 100 kHz.

B.5. Infrared cameras (IR)

Several IR cameras are available at MAST-U, we employ the systems located at the upper-outer and lower-outer divertors [76, 77]. The THEODOR code [78] is used to infer the peak heatflux q_{peak} [MWm^{-2}] from the IR images. As this code solves the heat equation for the divertor target plates, it also compensates for any dynamics related to the target plates warming up throughout a shot. For the shots considered in this paper, the strikepoint is often located near the transition from one divertor tile to another (T4 to T5, see figure B1). This, combined with field-ripple effects, may have caused the absolute value of the inferred peak heat flux to be inaccurate. Nevertheless, the peak heatflux for different perturbations can still be compared relative to each other. For most experiments considered in this work, the cameras used a reduced frame size to achieve an increased acquisition frequency of 1.25 kHz. Other, earlier, shots use a 400 Hz acquisition frequency.

B.6. Interferometry (IF)

The midplane laser interferometer [79] is used to measure the line-integrated core electron density. We mainly employ this diagnostic to keep track of the increasing core density throughout the shot. The applied vertical plasma position perturbations are often also evident in the IF signal, likely due to the plasma shifting more in and out of static line-of-sight.

B.7. Effect of divertor leg movement

A major concern in these experiments is the position of the divertor legs and their corresponding strike points as it was observed that the Z_{ref} perturbation also affects the divertor magnetic configuration. We illustrate this in figure B1 where we overlay the EFIT++ magnetic equilibrium for #49062c for all timeslices during which the perturbation is applied. Here, we can observe that, in addition to the intended movement of the plasma core, the divertor leg position also varies. Note that EFIT++ may give a conservative view of the movement of the divertor leg, as discussed in section 5. To minimise influence of the divertor leg movement on the imaging measurements, we take the intensity measurements (HSV, I_{sp}) in a larger area centred around the median position of the strike point. For the same reason, we take the D_2 Fulcher front position (L_x) w.r.t the X-point instead of the target as shown in other publications [53, 65, 35]. The divertor leg was found to be continuously in view of both IR cameras. For the line-of sight measurements (D-alpha, UFDS) the divertor leg was always in view of the sight-cones of both diagnostics, as illustrated in figure B1.

Appendix C. Post-processing

Proper synchronisation of the considered diagnostics is crucial for an accurate dynamic analysis. Also, the frequency response is affected by ELMs, which need to be filtered out. In this appendix, we illustrate both processes.

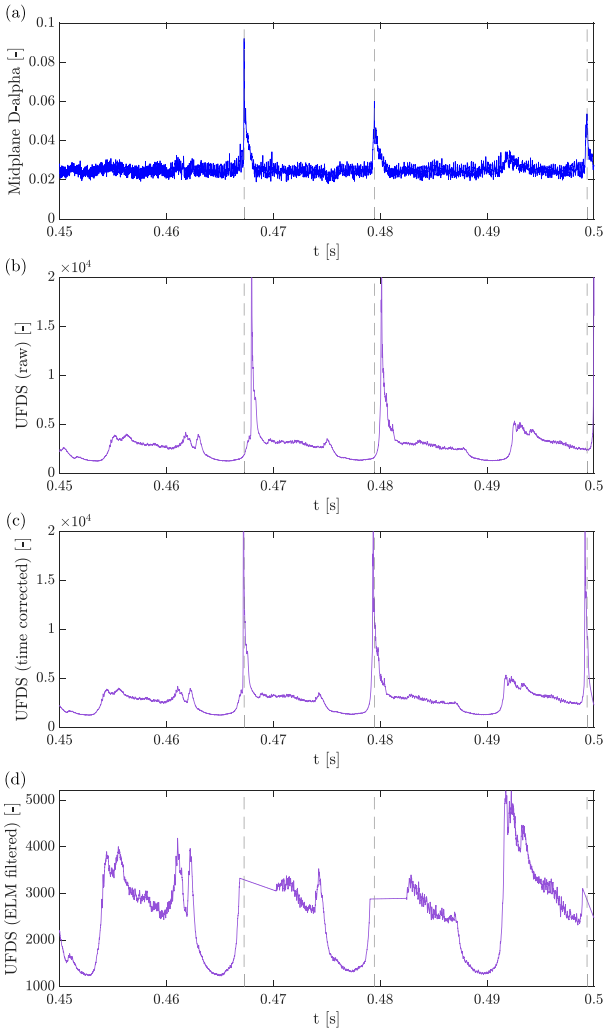

Figure C1. Illustration of timing and ELM corrections applied to the UFDS data for #49059. (*a*) The midplane D-alpha signal is used to detect ELMs, indicated by the dashed vertical lines. (*b*) The raw UFDS signal. (*c*) The UFDS signal with a timing correction applied, matching the ELM peaks. (*d*) Timing corrected UFDS signal with ELMs replaced by a linear interpolation.

C.1. Timing corrections

The timing has been verified for every diagnostic shown in this work. To this end, we have used the ELMs which are occasionally exhibited by the core plasma. The main assumption in this analysis is that the ELMs show up at each diagnostic simultaneously.

We illustrate this for the UFDS in figure C1 for #49059. In figure C1(*a*), we plot the midplane D-alpha filterscope signal, showing the ELMs as clearly recognisable peaks. The detected ELM peaks are indicated by the dashed vertical lines. The raw UFDS signal is shown in figure C1(*b*), here, the corresponding ELM peaks are also clearly recognisable. However, we observe a timing offset w.r.t. the ELM peaks from the midplane D-alpha filterscope. This is attributed to a drift in the internal diagnostic clock.

The timing of the UFDS and HSV1 required corrections, the ELM peaks in all other diagnostics were found to align

with the midplane D-alpha filterscope. For UFDS, a time vector scaling of 0.99 804 followed by a timeshift of 0.1595 ms is employed. For the HSV1, a timeshift of 1 ms is applied, consistent with a shift of one timestamp.

C.2. ELM filtering

Some of the shots considered contain ELMs, while others are ELM-free. These ELMs are not periodic and are therefore unrelated to the applied perturbations. The ELMs are filtered from the diagnostic signals to prevent their, often substantial, disturbance of the frequency response. We define a window around each ELM peak time t_{elm}, defined as the time span around a given ELM in which the signal is influenced significantly. For the UFDS signal shown in figure C1, this window is chosen as $[t_{\mathrm{elm}} - 0.4\,\mathrm{ms}, t_{\mathrm{elm}} + 3\,\mathrm{ms}]$. The data in the ELM window is replaced by a linear interpolation as the DFT requires evenly spaced sampling. The filtered signal is illustrated in figure C1(*d*).

Appendix D. ΔR_{sep} extraction

The ΔR_{sep} traces shown in this work arise from a combination of the EFIT++ magnetic equilibrium reconstruction and the vertical control system signals, as discussed in section 2.2. In this appendix, we illustrate this process.

The vertical plasma position Z is available through the EFIT++ magnetic equilibrium reconstruction as Z_{EFIT} at a sampling frequency of 1 kHz. We also extract the vertical plasma position according to the vertical control system as $Z_{\mathrm{VC}} = ZIp_{\mathrm{VC}}/Ip$, with Ip as the core plasma current and ZIp_{VC} as the combined plasma current and vertical position signal as used in the vertical control system. The resulting Z_{VC} signal has a sample frequency of 1 MHz. Both signals are shown for #49262 in figure D1(*a*). It is noted that the solenoid swing induces a drift in the measurement of Z_{VC}, i.e. the deviation between Z_{VC} and Z_{EFIT} varies during each shot, see figure D1(*a*).

ΔR_{sep} is available as well through EFIT++ as $\Delta R_{\mathrm{sep,EFIT}}$, also using a sampling frequency of 1 kHz. This signal is shown in figure D1(*b*). To increase the sampling frequency of $\Delta R_{\mathrm{sep,EFIT}}$, we rescale Z_{VC} to $\Delta R_{\mathrm{sep,EFIT}}$, utilising a scale and shift factor. Effectively, we are therefore using the shape of Z_{VC} to fill the datapoints in between $\Delta R_{\mathrm{sep,EFIT}}$. For the ramp towards USN shown in figure D1, we only consider the ramp itself (between the red lines) in the analysis presented in this paper (see figure 11). Therefore, we tune the scale and shift factors to achieve the best possible fit for this region.

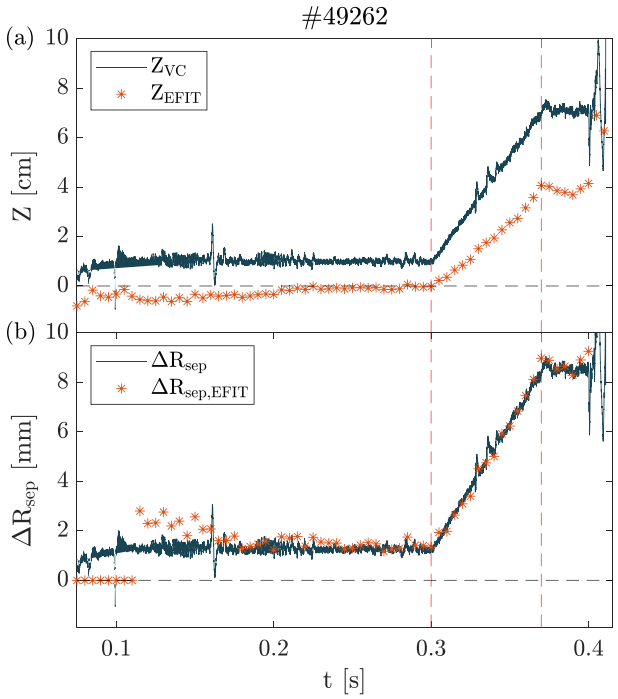

Figure D1. Computation of ΔR_{sep} for #49262, featuring a slow ramp towards USN. (*a*) The Z position from the vertical control Z_{VC} (1 MHz) and the EFIT++ magnetic reconstruction Z_{EFIT} (1 kHz). (*b*) ΔR_{sep} from EFIT++ $\Delta R_{\mathrm{sep,EFIT}}$ (1 kHz) and the ΔR_{sep} signal achieved by scaling and shifting Z_{VC} (1 MHz). The red lines indicate the ramp section of the experiment shown in figure 11, only this section is used to compute ΔR_{sep}.

The ΔR_{sep} computation is illustrated for the dynamic shot #49059a in figure D2. We tune the shift factors in 50 ms intervals to correct for drifts between Z_{VC} and $\Delta R_{\mathrm{sep,EFIT}}$. The resulting frequency response is shown in figure D2(*d*). As ΔR_{sep} is actuated through the vertical controls system as discussed in section 2.2, some noise is present. Nevertheless, the exited frequency f_{exc} is at least two orders of magnitude above the noise floor and is therefore clearly recognisable. This is also illustrated by the time domain evaluation of the response at f_{exc} in figure D2(*c*), clearly being the dominant contribution in the signal. Note that this example features the highest perturbation frequency considered at 200 Hz. Other shots which feature a lower perturbation frequency achieve an even clearer response.

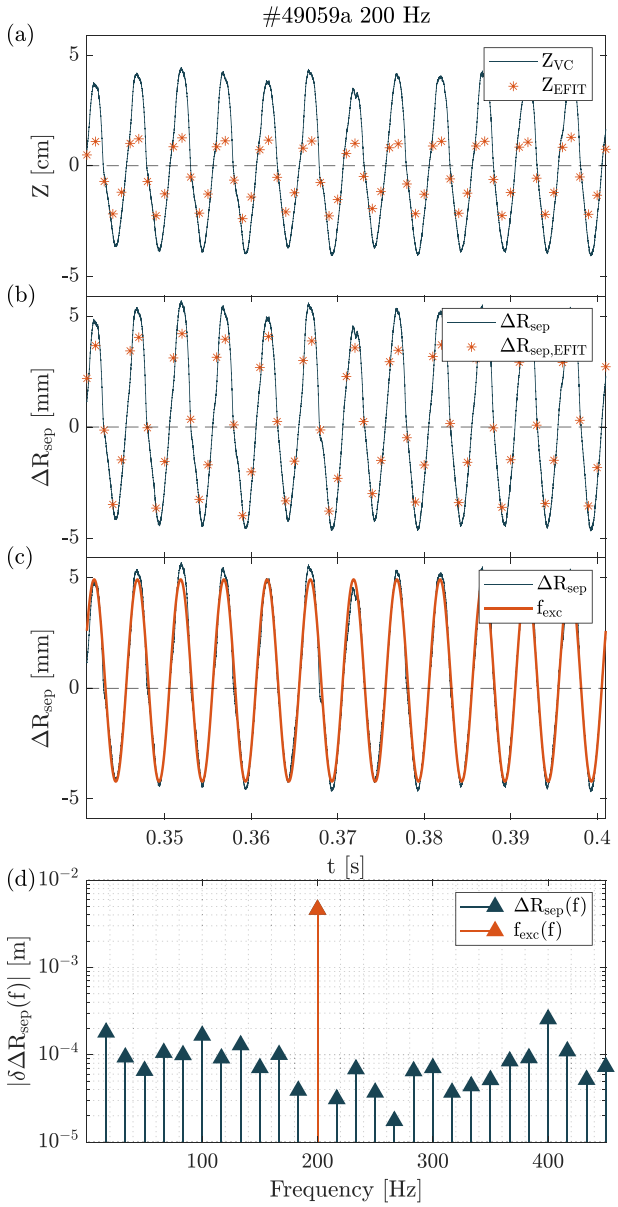

Figure D2. Computation of ΔR_{sep} for #49059a, featuring a 200 Hz perturbation frequency. (*a*) The Z position from the vertical control Z_{VC} (1 MHz) and the EFIT++ magnetic reconstruction Z_{EFIT} (1 kHz). (*b*) ΔR_{sep} from EFIT++ $\Delta R_{sep,EFIT}$ (1 kHz) and the ΔR_{sep} signal achieved by scaling and shifting Z_{VC} (1 MHz). (*c*) ΔR_{sep} and the time domain evaluation of the exited frequency f_{exc}. (*d*) Frequency domain response of ΔR_{sep} with f_{exc} shown in orange.

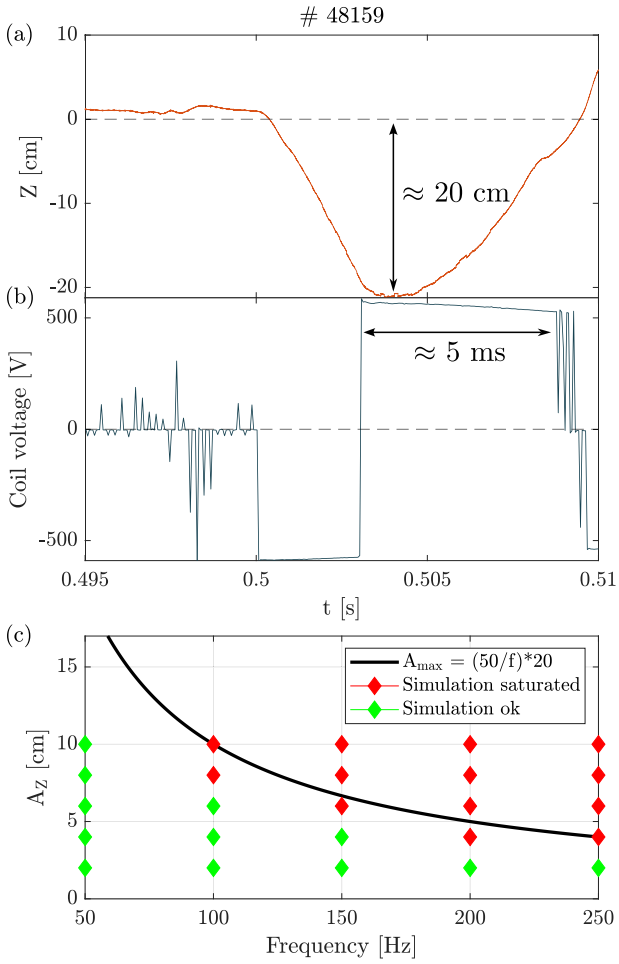

Figure E1. Extraction of vertical control system capabilities from vertical kick experiment #48159 and feedback control simulations. (*a*) Vertical position change as a result of the applied vertical kick, approximately 20 cm amplitude is achieved. (*b*) Applied vertical kick coil voltage, lasting approximately 5 ms. (*c*) Resulting vertical control capability curve $A_{max} = (50/f) * 20$, indicating the theoretical maximum amplitude for each frequency. Feedback simulations of the RZIp vertical control model [50, 80] are overlayed, indicating if the coil voltage saturates in trying to achieve the requested amplitudes for each frequencies.

Appendix E. Vertical control system limits

In this appendix, we explore the limits of the vertical control system to guide the design of the power-sharing perturbation signals. This occurred before the experiments shown in this paper were conducted.

We consider #48159 in which a vertical kick was applied to the plasma. During a vertical kick, the vertical control coils exert their maximum actuation force on the plasma column, directed either fully upwards or fully downwards. The coil voltage is shown in figure E1(*b*), the resulting vertical position response is displayed in figure E1(*a*). We note that a vertical displacement of approximately 20 cm was achieved while taking approximately 5 ms to transition back to a balanced configuration. This can be interpreted as one quarter of a sinusoidal perturbation. Hence, if this a perturbation is repeated, a sinusoid of approximately $1/(4 * 0.005) = 50$ Hz would result with an amplitude of approximately 20 cm. The achievable amplitude and frequency are interchangeable, i.e. higher amplitudes can be achieved at lower frequencies while higher frequencies can be achieved when using lower amplitudes. We can therefore define a vertical control capability curve as $A_{max} = (50/f) * 20$. This curve is plotted in figure E1(*c*) and serves as our simple approximation of the, theoretical, maximum amplitude and frequency the MAST-U vertical control system could to achieve, using maximum actuation at all times.

Simulations with the RZIp MAST-U vertical control system model [50, 80] are also performed. In addition to being

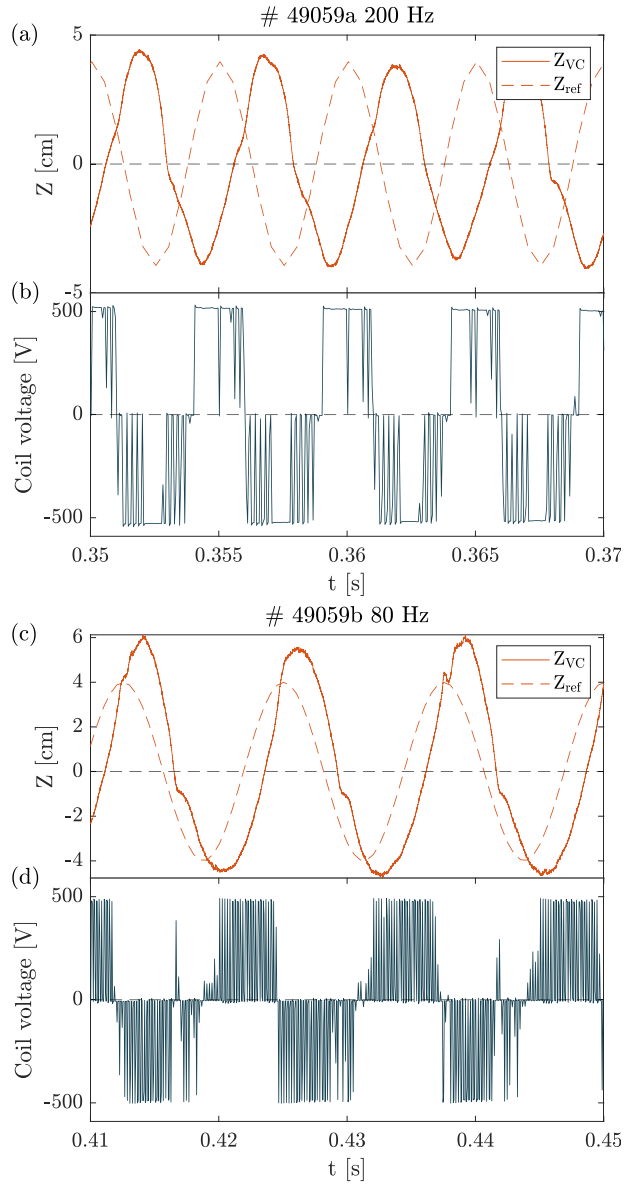

Figure E2. Vertical control system performance for 200 Hz (*a*), (*b*) and 80 Hz (*c*), (*d*) perturbations with $A_Z = 4$ cm, showing how 200 Hz is at the limit of vertical control system capability. (*a*), (*c*) Vertical position Z_{VC} as measured by the vertical control system and the requested reference trace Z_{ref}. (*b*), (*d*) Applied vertical control coil voltage, continuously switching between minimum and maximum through pulse-width modulation, relying on coil inductance to achieve a smooth response in coil current. Note how the voltage in the 200 Hz perturbation is applied almost continuously during each upwards or downwards part of the perturbation, i.e. maximum actuation force is applied almost continuously.

a more accurate representation of the system dynamics compared to the simple vertical control capability curve, this model also includes the vertical controller. Various amplitudes and frequencies are applied to this Linear-Time-Invariant RZIp model to gauge the limits of the vertical control system. The results are shown in figure E1(*c*), here, points where the simulated vertical control voltage demand is continuously at the $+-600$ volt limit are indicated as 'saturated'. The RZIp model also clearly indicates the trade-off between frequency and amplitude as predicted by the theoretical curve.

We observe in figure E1(*c*) how the achievable amplitudes from the RZIp simulation are slightly lower compared to the theoretical maximum, however, it is striking how well the simple theoretical approximation works. This theoretical curve, supported by the RZIp simulations, has guided the selection of the perturbation amplitudes for this work (table 1).

We now explore the vertical control system performance during sinusoidal perturbations. The voltage in the vertical control coils switches between minimum and maximum, applied through pulse-width modulation, relying on coil inductance to achieve a smooth response in coil current. In figures E2 we display the vertical performance for a perturbation frequency of 200 Hz (#49059a, figure E2(*a*) and (*b*)) and 80 Hz (#49059b, figures E2(*c*) and (*d*)), both using the same 4 cm amplitude. Note how the voltage for the 200 Hz perturbation is applied almost continuously during each upwards and downwards part of the perturbation, i.e. maximum actuation force is applied almost continuously. This is not the case for the 80 Hz perturbation, showing how the 80 Hz perturbation request is significantly easier for the vertical control system to follow. Using an amplitude of 4 cm, 200 Hz is highest perturbation frequency which can be achieved using the MAST-U vertical control system in this particular plasma scenario. This is in remarkable agreement with the RZIp simulations and the theoretical vertical control curve in figure E1(*c*), indicating how such methods are highly valuable to gauge the limits of the vertical control system *a priori* to guide the design of perturbation signals.

Appendix F. HSV1 ROI

The HSV1 D-alpha filtered camera system views the MAST-U plasma core from the midplane, covering both inner targets, see figure B1(*a*). In our analysis, we select dedicated ROIs for the upper-inner and lower-inner targets and take the sum of the pixel intensity in each. The precise location of the ROIs was observed to greatly influence the resulting signal, this is discussed in this appendix.

In figure F1, we show the HSV1 response for various ROIs for the balanced equilibrium experiment #49059b, using a 40 Hz perturbation, with the dashed lines indicating the peaks of the applied ΔR_{sep} perturbation. The lower-inner strikepoint region (*a*) clearly exhibits a response to the applied perturbation. The response for the upper-inner strikepoint region (*b*) appears to be attenuated. We observe a response which is 180 degrees out of phase with the lower strikepoint in region (*a*) as expected. A second effect, in phase with the lower strikepoint, can also be observed. Region (*c*) appears to only show this second effect while region (*d*), located even further away from the strikepoint, does not show a recognisable response to the perturbation. The attenuation of the strikepoint response due to this second effect was observed most clearly in the upper divertor for the downshifted shots, perhaps as the power making its way to the upper-inner divertor is smallest

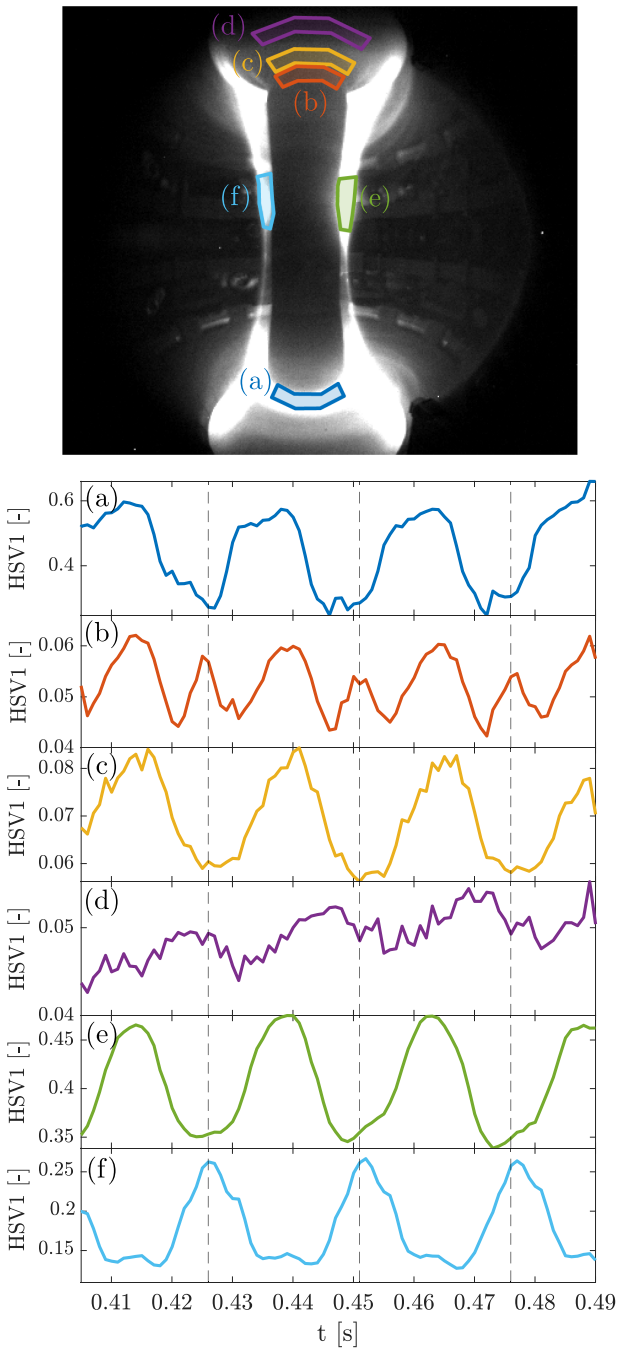

Figure F1. HSV1 response for various regions of interest (ROIs) for balanced equilibrium #49059b, using a 40 Hz perturbation. The dashed lines indicate the peaks of the applied ΔR_{sep} perturbation. (*a*) Lower-inner divertor strikepoint, showing a clearly recognisable response. (*b*) Upper-inner strikepoint which appears to be attenuated by an unknown effect. (*c*) Upper-inner divertor response which, unexpectedly, is in phase with the lower-inner strikepoint response in (*a*). (*d*) Upper-inner divertor region which does not show a clearly recognisable response. The response in Regions (*e*) and (*f*) located in opposed toroidal locations is in anti-phase for an unknown reason.

in those cases. Nevertheless, the effect is noticeably present in both the upper and lower targets for both balanced and downshifted experiments. For this reason, the upper data available for the inner target in figure 9 is very limited, especially for the low frequency points which primarily employ down-shifted equilibria.

Next, we compare regions (*e*) and (*f*), located on opposing toroidally opposed positions, near the employed fuelling valve. We see that the response in both regions is in anti-phase. This is intriguing, as one would assume the applied vertical plasma perturbations to result in a toroidally symmetric response. This might be explained by the presence of a horizontal plasma perturbation as a side effect of the applied vertical perturbation, perhaps also connected to the strikepoint attenuation affect mentioned above. The exact origin of this effect remains unknown, it is observed across all experiments, both balanced and downshifted.

For all data shown throughout this paper, the ROI was always kept strictly restricted to the precise strikepoint location. In figure F1, this corresponds to regions (*a*) and (*b*). Small differences in camera alignment and the strikepoint location necessitated the ROIs to be tuned individually for each shot.

Appendix G. Variations between experiments

Variations in divertor response are occasionally observed between experiments, for the same divertor and diagnostic. This is discussed in this appendix. We explicitly consider the effect of the amplitude of the applied ΔR_{sep} perturbation on observed divertor response.

A comparison of the lower-outer divertor UFDS response is shown for two different experiments in figure G1. The relatively linear time and frequency domain response for the downshifted perturbation #48648a is displayed in figure G1(*a*). Note how the output response at harmonics of the excited frequency are relatively small in comparison to the linear response at the excited frequency itself. This is also evidenced in figure G1(*b*), here, the response is dominantly linear, although the signals appears to follow a distinctly different slope for upwards perturbation (coloured dots) and downwards perturbations (white dots).

Contrary to this, we show a highly non-linear UFDS response for #49062b in figure G1(*c*). Note how the response at the harmonics of the excited frequency have a comparable magnitude to the output response at the excited frequency. Consequently, the time domain representation of the output response at the excited frequency no longer resembles the actual output signal. The corresponding plot of the UFDS signal as function of ΔR_{sep} in figure G1(*d*) also illustrates this behaviour as there is no longer a recognisable pattern in the output signal.

The perturbations employed in our experiments feature a variety of different ΔR_{sep} amplitudes. In figure G2, we show the upper-outer divertor D_{alpha} response as function of ΔR_{sep} for shot #48648b featuring a 40 Hz perturbation. This is a downshifted perturbation, with the largest ΔR_{sep} deviation of all shots with $A_{\max,\Delta R_{\text{sep}}} = 15.2$, see table 1. We observe a change-in-slope in the D_{alpha} response as function of ΔR_{sep}. We observe how the slope is significantly steeper near a balanced configuration (A) compared to a deeply downshifted configuration (B), and appears to saturate towards LSN. This might be explained by the fact that the sensitivity to ΔR_{sep}

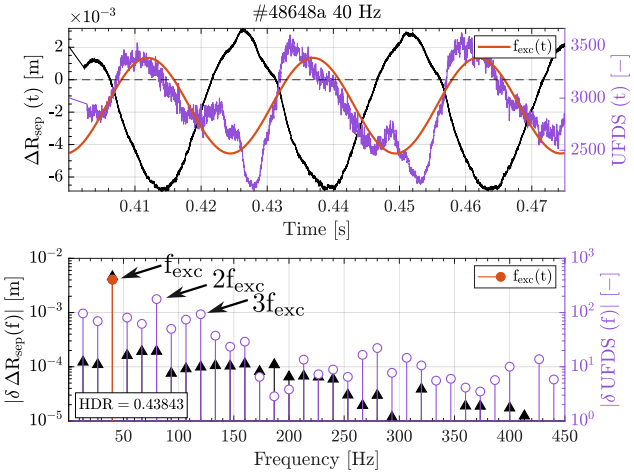

(a) Lower-outer divertor UFDS response in time and frequency domain, #48648a

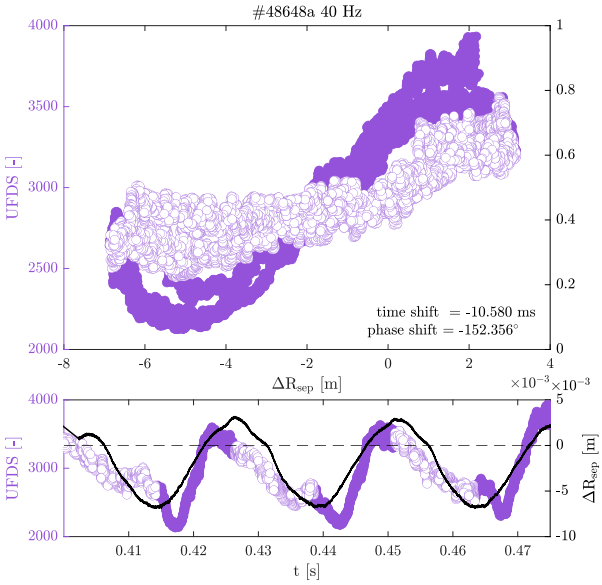

(b) Lower-outer divertor UFDS response in time domain and as function of ΔR_{sep}, #48648a

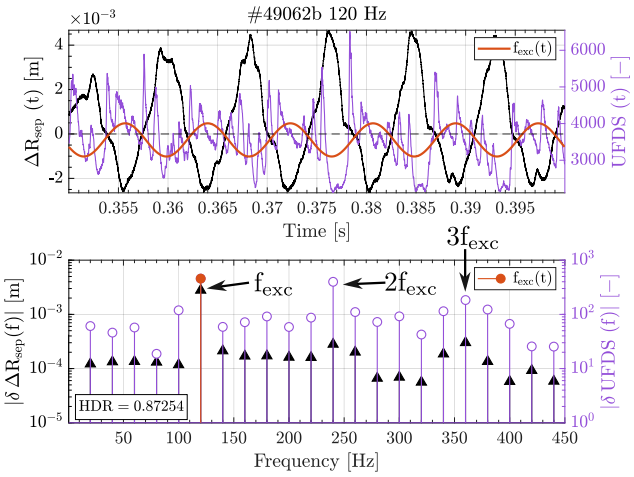

(c) Lower-outer divertor UFDS response in time and frequency domain, #49062b

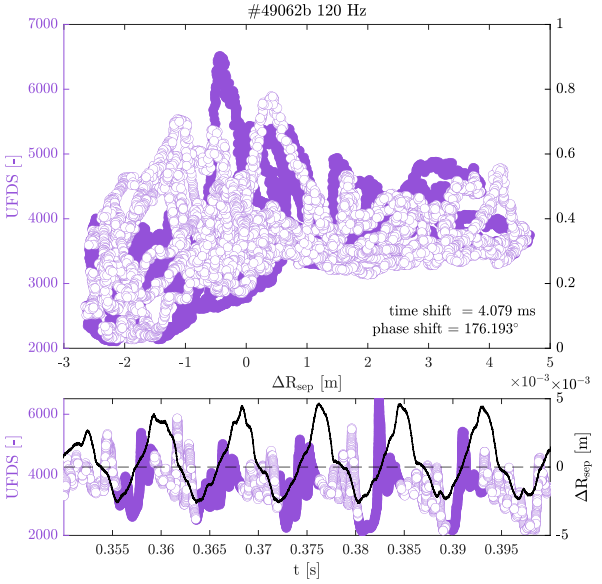

(d) Lower-outer divertor UFDS response in time domain and as function of ΔR_{sep}, #49062b

Figure G1. Differences in linearity between experiments #48648a (*a*), (*b*) and #49062b (*c*), (*d*), with the latter showing a significantly more non-linear UFDS D_2 Fulcher band response. Figures (*a*) and (*c*) show the time domain (upper) and frequency domain (lower) response, including an overlay of the applied ΔR_{sep} input signal (black), the output response at the excited frequency (orange), and the Harmonic Distortion Ratio (HDR). Figures (*b*) and (*d*) show the UFDS response as function of ΔR_{sep} and in time domain with the indicated phase correction applied (or equivalent timeshift). The coloured and white dots indicate a positive and negative ΔR_{sep} movement respectively .

perturbations necessarily decreases for larger ΔR_{sep} since, once a fully LSN configuration is reached, decreasing ΔR_{sep} even further has no further effect on the power-sharing. This might be related to the occasional observation of non-linear behaviour as discussed in section 3.2. This effect is present in other shots as well, but is most clear in #48648b as it covers the largest ΔR_{sep} range.

Interestingly, this behaviour seems to align with the power-sharing predicted by the Brunner model [28], see figure G3. The model also predicts a saturation in power fraction for large ΔR_{sep} values, although the exact point where this occurs is subject the selected parameters. To generate this figure, we employ the parameters specified in table 3 which carry significant uncertainty. Note how the ΔR_{sep} range covered

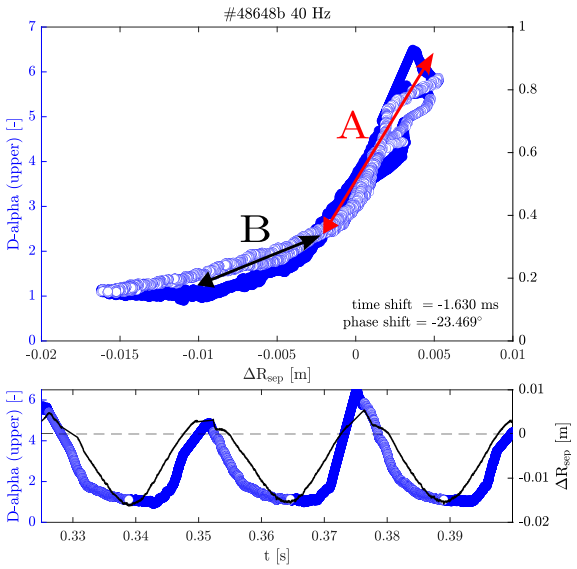

Figure G2. Upper-outer divertor D-alpha response in time domain and as function of the applied ΔR_{sep} input for a downshifted 40 Hz perturbation #48648b, the applied phase correction is indicated as well as the equivalent timeshift. The slope of the curve is significantly steeper near a balanced configuration (A) compared to a more downshifted configuration (B).

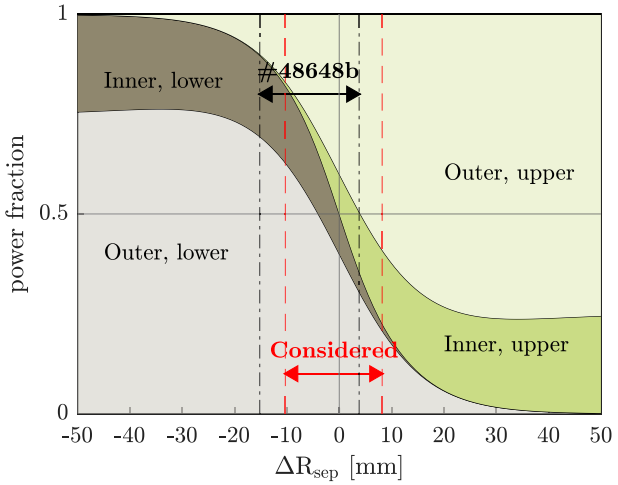

Figure G3. Power-sharing as function of ΔR_{sep} according to the Brunner model [28] using the parameters specified in table 3. Each coloured area corresponds to one of the four targets as indicated. The arrows indicates the predominantly linear ΔR_{sep} range considered in our analysis (red) and the larger range covered in #48648b (black).

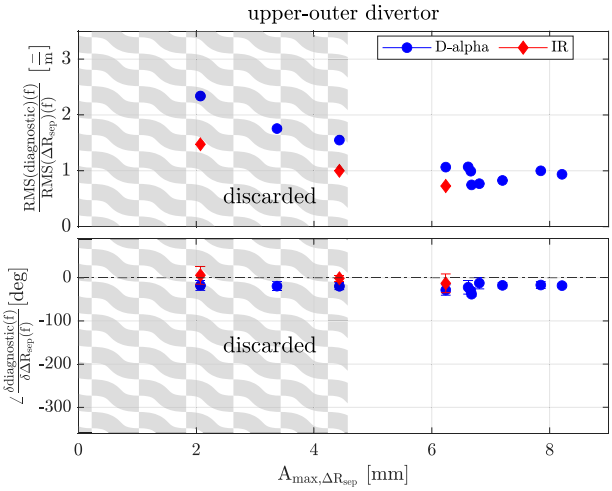

Figure H1. Upper-outer divertor D-alpha and IR magnitude and phase response for shots with various $A_{\max,\Delta R_{\text{sep}}}$, all considered shots use the same 120 Hz perturbation frequency. We observe an increased magnitude response for perturbations with small $A_{\max,\Delta R_{\text{sep}}}$.

in #48648b creeps into the non-linear power-sharing range, aligning with the observations in figure G2.

Let us consider the influence of the change-in-slope on the gain and phase response of the outer divertors in figure H1. All experiments in this figure feature the same 120 Hz perturbation frequency, but vary greatly in perturbation amplitude. Note how datapoints which have a small $A_{\max,\Delta R_{\text{sep}}}$ amplitude feature the highest gain, corresponding to region A in figure G2. For $A_{\max,\Delta R_{\text{sep}}} > 4.5$ mm, we observe a similar gain, i.e. the ratio between the input and output signals is roughly the same regardless of amplitude.

The applied amplitude therefore has a major effect on the observed divertor response. For this reason, we restrict our analysis to a comparable set of amplitudes in the linear regime, see appendix H.

Appendix H. Applied thresholds

In this appendix, we discuss the various thresholds applied to the data in this study to ensure the most fair and consistent comparison possible.

As discussed in appendix G, the selected amplitude has a major effect on the divertor response. Ideally, multiple frequency scans would have been performed at various amplitudes to facilitate a complete comparison, the available data

is however limited. Therefore, to avoid distortions in the Bode plots, we only consider the experiments with $A_{\max,\Delta R_{\text{sep}}} > 4.5$ mm in the remainder of this paper, i.e. the non-shaded region in figure H1. All discarded datapoints are shown in the shaded region. Note that this retains the most important dataset as, essentially, we are interested most in the dynamics for configurations with $\Delta R_{\text{sep}} > \lambda_q/2$ as dynamical effects might alleviate their power-sharing imbalance. For MAST-U with $\lambda_q \approx 8$ mm [67], we therefore focus on this range with the applied $A_{\max,\Delta R_{\text{sep}}} > 4.5$ mm threshold. However, as discussed in appendix G, the largest ΔR_{sep} amplitude applied in #48648b starts to reach into the power-sharing saturation region. Therefore, we remove this shot from our frequency domain analysis by applying an upper limit $A_{\max,\Delta R_{\text{sep}}} < 11$ mm. The considered ΔR_{sep} range is shown in figure G3. Note how it is almost exclusively restricted to the linear regime of the Brunner model.

For a dominantly linear system, the phase delay is clearly defined as illustrated in figure 4. However, for a system with highly non-linear contributions, the definition of a phase shift starts to break down. For example, compare figures G1(a) and (c), the latter does not show a clearly recognisable phase. Therefore, in the Bode plots shown in this paper, we discard the phase for datapoints where the HDR indicates that the response is not dominantly linear. We have chosen HDR $<$ 0.65 as the requirement to show the phase response for every datapoint.

Furthermore, we only consider datapoints which have at least 4 samples per period. Otherwise, the observed phase and RMS would be distorted since they become highly sensitive to the, often substantial, noise level. Also, we require a minimal SNR of 5 [56], extracted from the LPM as discussed in [81].

In conclusion, for all Bode plots shown in this paper, the following thresholds are applied:

- HDR < 0.65 (only phase)
- $\frac{f_{\text{diag}}}{f_{\text{exc}}} > 4$ (gain and phase)
- $4.5\,\text{mm} < A_{\max,\Delta R_{\text{sep}}} < 11\,\text{mm}$ (gain and phase)
- SNR > 5 (gain and phase).

Appendix I. Balanced versus down-shifted

The results presented in this paper occasionally show a large scatter in the phase response. In this appendix, we discuss the balancedness of the equilibrium as a potential factor.

A comparison between the outer divertor frequency response functions for balanced and down-shifted perturbations is shown in figure I1. Note that this features the exact same datapoints as shown in figure 6. For the upper-outer divertor in figure I1(a), we observe that the phase response is similar between both configurations. This is expected since the scatter in phase response in figure 6(b) is minimal.

For the lower-outer divertor, the down-shifted configurations (red) appear to show a reduced phase delay w.r.t. the balanced configurations (green). This effect is present in both figure I1(b) (D-alpha and IR) as well as figure I1(c) (UFDS, L_x, L_{sp}). It appears to manifest mainly at higher frequencies,

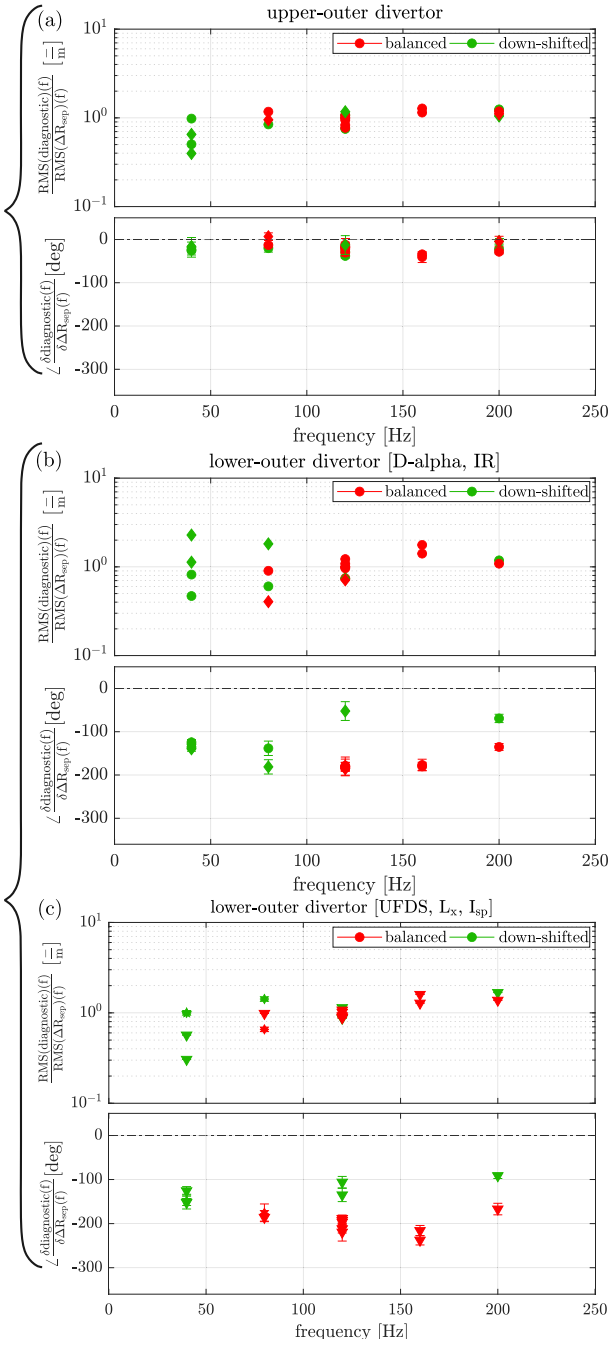

Figure I1. Comparison of the outer divertor power-sharing dynamics between balanced and down-shifted configurations, note that the exact same data is also presented in figure 6. (a) Upper-outer divertor D-alpha and IR response, showing comparable results between both configurations. (b) Lower-outer divertor D-alpha and IR response where the down-shifted equilibria appear to show a reduced phase delay. This also applies to the UFDS, L_x, and L_{sp} response shown in (c).

but this is likely influenced by the fact that most of the lower frequency shots feature only down-shifted equilibria. No such effect was observed for the inner divertors, perhaps in part due to the reduced dataset.

The exact reason for this effect remains unclear at present. A promising next step would be to perform experiments with

up-shifted perturbations to determine whether the observed trend persists. If it does not, the effect is likely due to an asymmetric mechanism such as drifts. Notably, it does not appear to influence the magnitude of the response. Nevertheless, it is a striking observation that warrants further investigation in future studies on DN power-sharing dynamics.

ORCID iDs

B. Kool 0000-0002-1636-7400
G.L. Derks 0000-0003-3420-0388
S.S. Henderson 0000-0002-8886-1256
J. Lovell 0000-0001-9565-3466
O.P. Bardsley 0000-0002-1525-675X
T.A. Wijkamp 0000-0003-3110-8682
P.A. Figueiredo 0009-0004-7052-6793
S. Silburn 0000-0002-3111-5113
N. Lonigro 0000-0001-8581-0384
K. Verhaegh 0000-0002-0500-2764
M. van Berkel 0000-0001-6574-3823

References

[1] Pitts R.A. *et al* 2019 Physics basis for the first ITER tungsten divertor *Nucl. Mater. Energy* **20** 100696
[2] Zohm H., Militello F., Morgan T.W., Morris W., Reimerdes H. and Siccinio M. 2021 The EU strategy for solving the DEMO exhaust problem *Fusion Eng. Des.* **166** 112307
[3] Henderson S.S. *et al* 2025 An overview of the STEP divertor design and the simple models driving the plasma exhaust scenario *Nucl. Fusion* **65** 016033
[4] Lennholm M. *et al* 2024 (the STEP Team) Controlling a new plasma regime *Phil. Trans. R. Soc. A* **382** 20230403
[5] Biel W. *et al* 2022 Development of a concept and basis for the DEMO diagnostic and control system *Fusion Eng. Des.* **179** 113122
[6] Baker A. 2024 The Spherical Tokamak for Energy Production (STEP) in context: UK public sector approach to fusion energy *Phil. Trans. R. Soc. A* **382** 20230401
[7] Muldrew S.I. *et al* 2024 Conceptual design workflow for the STEP prototype powerplant *Fusion Eng. Des.* **201** 114238
[8] Sorbom B.N. *et al* 2015 ARC: a compact, high-field, fusion nuclear science facility and demonstration power plant with demountable magnets *Fusion Eng. Des.* **100** 378–405
[9] Creely A.J. *et al* (the SPARC Team) 2020 Overview of the SPARC tokamak *J. Plasma Phys.* **86** 865860502
[10] Windridge M. 2020 Tokamak Energy *Commercialising Fusion Energy* ed W.J. Nuttall, S. Konishi, S. Takeda and D. Webbe-Wood (IOP Publishing) pp 5-1–15
[11] Wilson H., Chapman I., Denton T., Morris W., Patel B., Voss G. and Waldon C. (the STEP Team) 2020 STEP—on the pathway to fusion commercialization *Commercialising Fusion Energy* (IOP Publishing) pp 8-1–18
[12] Whyte D.G., Minervini J., LaBombard B., Marmar E., Bromberg L. and Greenwald M. 2016 Smaller & sooner: exploiting high magnetic fields from new superconductors for a more attractive fusion energy development path *J. Fusion Energy* **35** 41–53
[13] Valanju P.M., Kotschenreuther M., Mahajan S.M. and Canik J. 2009 Super-X divertors and high power density fusion devices *Phys. Plasmas* **16** 056110
[14] Havlíčková E., Wischmeier M., Lipschultz B. and Fishpool G. 2015 The effect of the Super-X divertor of MAST Upgrade on impurity radiation as modelled by SOLPS *J. Nucl. Mater.* **463** 1209–13
[15] Moulton D., Harrison J.R., Xiang L., Ryan P.J., Kirk A., Verhaegh K., Wijkamp T.A., Federici F., Clark J.G. and Lipschultz B. 2024 Super-X and conventional divertor configurations in MAST-U ohmic L-mode; a comparison facilitated by interpretative modelling *Nucl. Fusion* **64** 076049
[16] Bernert M. *et al* 2021 X-point radiation, its control and an ELM suppressed radiating regime at the ASDEX Upgrade tokamak *Nucl. Fusion* **61** 2021
[17] Bernert M. *et al* 2023 The X-Point radiating regime at ASDEX Upgrade and TCV *Nucl. Mater. Energy* **34** 101376
[18] Meyer H. 2022 The physics of the preferred plasma scenario for STEP *48th EPS Conf. on Plasma Physics* (available at: https://scientific-publications.ukaea.uk/wp-content/uploads/UKAEA-STEP-CP2307.PDF/)
[19] Kuang A.Q. *et al* 2018 Conceptual design study for heat exhaust management in the ARC fusion pilot plant *Fusion Eng. Des.* **137** 221–42
[20] Reimerdes H. *et al* 2020 Assessment of alternative divertor configurations as an exhaust solution for DEMO *Nucl. Fusion* **60** 066030
[21] Aho-Mantila L. *et al* 2021 Scoping the characteristics and benefits of a connected double-null configuration for power exhaust in EU-DEMO *Nucl. Mater. Energy* **26** 100886
[22] Smick N., LaBombard B. and Hutchinson I.H. 2013 Transport and drift-driven plasma flow components in the Alcator C-Mod boundary plasma *Nucl. Fusion* **53** 023001
[23] Harrison J.R., Bowman C., Clark J.G., Kirk A., Lovell J., Patel B.S., Ryan P., Scannell R., Thornton A.J. and Verhaegh K. 2024 Benefits of the Super-X divertor configuration for scenario integration on MAST Upgrade *Plasma Phys. Control. Fusion* **66** 065019
[24] Verhaegh K. *et al* (the Mast Upgrade Team) 2023 Spectroscopic investigations of detachment on the MAST Upgrade Super-X divertor *Nucl. Fusion* **63** 016014
[25] Dreval M.B. *et al* (the MAST-U Team) 2025 Observation of bi-directional global Alfvén eigenmodes in the MAST-U tokamak *Nucl. Fusion* **65** 016043
[26] Lennholm M. *et al* 2024 Plasma control for the step prototype power plant *Nucl. Fusion* **64** 096036
[27] Osawa R.T., Moulton D., Newton S.L., Henderson S.S., Lipschultz B. and Hudoba A. 2023 SOLPS-ITER analysis of a proposed STEP double null geometry: impact of the degree of disconnection on power-sharing *Nucl. Fusion* **63** 076032
[28] Brunner D., Kuang A.Q., LaBombard B. and Terry J.L. 2018 The dependence of divertor power sharing on magnetic flux balance in near double-null configurations on Alcator C-Mod *Nucl. Fusion* **58** 076010
[29] Février O. *et al* (the TCV Team) 2021 Detachment in conventional and advanced double-null plasmas in TCV *Nucl. Fusion* **61** 116064
[30] Walker M.L. and Humphreys D.A. 2009 On feedback stabilization of the tokamak plasma vertical instability *Automatica* **45** 665–74
[31] Pesamosca F., Felici F. and Coda S. 2022 (the TCV Team) Improved plasma vertical position control on TCV using model-based optimized controller synthesis *Fusion Sci. Technol.* **78** 427–48
[32] Eich T. *et al* 2013 Scaling of the tokamak near the scrape-off layer H-mode power width and implications for ITER *Nucl. Fusion* **53** 093031
[33] Donné A.J.H., Costley A.E. and Morris A.W. 2012 Diagnostics for plasma control on DEMO: challenges of implementation *Nucl. Fusion* **52** 074015

[34] Anand H., Bardsley O., Humphreys D., Lennholm M., Welander A., Xing Z., Barr J., Walker M., Mitchell J. and Meyer H. 2023 Modelling, design and simulation of plasma magnetic control for the Spherical Tokamak for Energy Production (STEP) *Fusion Eng. Des.* **194** 113724
[35] Ravensbergen T. *et al* 2021 Real-time feedback control of the impurity emission front in tokamak divertor plasmas *Nat. Commun.* **12** 2021
[36] van Berkel M., Bosman T.O.S.J., Derks G.L., Koenders J.T.W. and Kool B. 2023 A model predictive control strategy for the exhaust *ITPA DivSOL* (*Oak Ridge National Laboratory, TN USA*, *June 2023*)
[37] Sarah L.N. *et al* 2022 Physics drivers of the STEP divertor concept design *4th Technical Meeting on Divertor Concepts, IAEA Headquarters* (available at: https://conferences.iaea.org/event/286/contributions/25131/contribution.pdf/)
[38] Petrie T.W. *et al* 2001 The effect of divertor magnetic balance on H-mode performance in DIII-D *J. Nucl. Mater.* **290–293** 935–9
[39] de Temmerman G., Delchambre E., Dowling J., Kirk A., Lisgo S. and Tamain P. 2010 Thermographic study of heat load asymmetries during MAST L-mode discharges *Plasma Phys. Control. Fusion* **52** 095005
[40] de Temmerman G., Kirk A., Nardon E. and Tamain P. 2011 Heat load asymmetries in MAST *J. Nucl. Mater.* **415** S383–6
[41] Kirk A. *et al* 2004 (the Mast Team) ELM characteristics in MAST *Plasma Phys. Control. Fusion* **46** 551–72
[42] Guo H.Y. *et al* 2011 Recent progress on divertor operations in EAST *J. Nucl. Mater.* **415** S369–74
[43] Moiraf D. *et al* 2025 Heat and particle exhaust in double-null configuration in WEST: experimental study and modeling with SOLEDGE-EIRENE *Nucl. Mater. Energy* **42** 101901
[44] Paradela Pérez I.P., Lomanowski B., Lore J.D., Lovell J. and Moulton D. 2025 Power balance and divertor asymmetries in the Super-X divertors of MAST-U using SOLPS-ITER* *Nucl. Fusion* **65** 066026
[45] Petrie T.W. *et al* 2019 High-performance double-null plasmas under radiating mantle scenarios on DIII-D *Nucl. Mater. Energy* **19** 267–72
[46] Lovell J., Henderson S.S., Stobbs J.M., Kirk A., Federici F., Patel B.S., Ryan P.J., Harrison J.R., Lomanowski B.A. and Lore J.D. 2024 Experimental investigation of steady state power balance in double null and single null H mode plasmas in MAST Upgrade *Nucl. Mater. Energy* **41** 101779
[47] Henderson S.S. *et al* 2024 Validating reduced models for detachment onset and reattachment times on MAST-U *Nucl. Mater. Energy* **41** 101765
[48] UKAEA 2019 MAST Upgrade Research Plan *Technical Report* Culham Centre for Fusion Energy (available at: https://ccfe.ukaea.uk/wp-content/uploads/2019/12/MAST-U_RP_2019_v1.pdf/)
[49] Wesson J. 2004 *Tokamaks* (Oxford University Press)
[50] Cunningham G. 2013 High performance plasma vertical position control system for upgraded MAST *Fusion Eng. Des.* **88** 3238–47
[51] Kogan L. *et al* 2022 First MAST-U Equilibrium Reconstructions using the EFIT++ code *48th EPS Conf. on Plasma Physics P2a.116* (available at: https://pure.tue.nl/ws/portalfiles/portal/274268100/P2a.116.pdf/)
[52] Berkery J.W., Sabbagh S.A., Kogan L., Ryan D., Bialek J.M., Jiang Y., Battaglia D.J., Gibson S. and Ham C. 2021 Kinetic equilibrium reconstructions of plasmas in the MAST database and preparation for reconstruction of the first plasmas in MAST Upgrade *Plasma Phys. Control. Fusion* **63** 055014
[53] Koenders J.T.W., Perek A., Kool B., Février O., Ravensbergen T., Galperti C., Duval B.P., Theiler C. and van Berkel M. 2023 Model-based impurity emission front control using deuterium fueling and nitrogen seeding in TCV *Nucl. Fusion* **63** 026006
[54] Koenders J.T.W., Wensing M., Ravensbergen T., Février O., Perek A. and van Berkel M. 2022 (the TCV Team and the EUROfusion MST1 Team) Systematic extraction of a control-oriented model from perturbative experiments and SOLPS-ITER for emission front control in TCV *Nucl. Fusion* **62** 066025
[55] Bosman T.O.S.J. *et al* (the ASDEX Upgrade Team, JET Contributors and the EUROfusion Tokamak Exploitation Team) 2025 X-point radiator control and its dynamics in ASDEX Upgrade and JET deuterium–tritium discharges *Nucl. Fusion* **65** 016057
[56] van Berkel M. 2015 Estimation of heat transport coefficients in fusion plasmas *Phd Thesis 1 (Research TU/e / Graduation TU/e)* Technische Universiteit Eindhoven Eindhoven (available at: https://pure.tue.nl/ws/portalfiles/portal/3837576/794807.pdf/)
[57] van Berkel M., Bosman T.O.S.J., Ceelen L., Derks G.L., Koenders J.T.W. and Kool B. 2025 Systematic multi-machine analysis of the exhaust time-dependent behavior in tokamaks *Nucl. Fusion* submitted
[58] Verhaegh K. *et al* 2021 A novel hydrogenic spectroscopic technique for inferring the role of plasma–molecule interaction on power and particle balance during detached conditions *Plasma Phys. Control. Fusion* **63** 035018
[59] Osborne N. *et al* (the MAST-U Team) 2024 Initial Fulcher band observations from high resolution spectroscopy in the MAST-U divertor *Plasma Phys. Control. Fusion* **66** 025008
[60] Pintelon R. and Schoukens J. 2012 *System Identification: A Frequency Domain Approach* (Wiley, Inc)
[61] van Berkel M. *et al* (the LHD Experiment Group and the TCV Team) 2020 Correcting for non-periodic behaviour in perturbative experiments: application to heat pulse propagation and modulated gas-puff experiments *Plasma Phys. Control. Fusion* **62** 094001
[62] Schoukens J., Vandersteen G., Barbé K. and Pintelon R. 2009 Nonparametric preprocessing in system identification: a powerful tool *Eur. J. Control* **15** 260–74
[63] Skogestad S. and Postlethwaite I. 2005 *Multivariable Feedback Control: Analysis and Design* (Wiley)
[64] Kool B. *et al* (the EUROfusion tokamak exploitation Team and the MAST-U Team) 2025 Demonstration of Super-X divertor exhaust control for transient heat load management in compact fusion reactors *Nat. Energy* **10** 1824
[65] Wijkamp T.A. *et al* (the MAST Upgrade Team) 2023 Characterisation of detachment in the MAST-U Super-X divertor using multi-wavelength imaging of 2D atomic and molecular emission processes *Nucl. Fusion* **63** 056003
[66] Verhaegh K. *et al* 2024 (the EUROfusion Tokamak Exploitation Team and the MAST-U Team) Investigations of atomic and molecular processes of NBI-heated discharges in the MAST Upgrade Super-X divertor with implications for reactors *Nucl. Fusion* **64** 086050
[67] Stobbs J.M. 2024 The infrared thermography system on the MAST-U tokamak *25th Topical Conf. on High Temperature Plasma Diagnostics (HTPD)* (*Asheville, TN USA*)
[68] Kukushkin A.S. and Krasheninnikov S.I. 2019 Bifurcations and oscillations in divertor plasma *Plasma Phys. Control. Fusion* **61** 074001
[69] Kembleton R., Siccinio M., Maviglia F. and Militello F. 2022 Benefits and challenges of advanced divertor configurations in DEMO *Fusion Eng. Des.* **179** 113120
[70] Verhaegh K. *et al* (the EUROfusion Tokamak Exploitation Team and the MAST Upgrade Team) 2025 Divertor shaping with neutral baffling as a solution to the tokamak power exhaust challenge *Commun. Phys.* **1** 215

[71] Morgan T.W., Li Y., Balden M., Brezinsek S. and De Temmerman G. 2021 Combined high fluence and high cycle number transient loading of ITER-like monoblocks in Magnum-PSI *Nucl. Fusion* **61** 116045
[72] Li Y., Morgan T.W., Van Dommelen J.A.W., Antusch S., Rieth M., Hoefnagels J.P.M., Terentyev D., De Temmerman G., Verbeken K. and Geers M.G.D. 2020 Fracture behavior of tungsten-based composites exposed to steady-state/transient hydrogen plasma *Nucl. Fusion* **60** 046029
[73] Breslau J., Gorelenkova M., Poli F., Sachdev J., Pankin A., Perumpilly G. and Yuan X. 2018 Laszlo Glant and USDOE Office of Science *TRANSP* (https://doi.org/10.11578/dc.20180627.4)
[74] Feng X. *et al* 2021 (MAST-U Team and EUROfusion MST1 Team) Development of an 11-channel multi wavelength imaging diagnostic for divertor plasmas in MAST Upgrade *Rev. Sci. Instrum.* **92** 063510
[75] Perek A. *et al* (TCV and EUROfusion MST1 Teams) 2019 MANTIS: a real-time quantitative multispectral imaging system for fusion plasmas *Rev. Sci. Instrum.* **90** 123514
[76] Andrew J.T., Elmore S., Fishpool G., Kirk A. and Liu Y.Q. (the MAST Team) 2015 Infrared measurements of divertor heat loads on MAST *2015 Int. Spherical Tokamak Workshop* (*Princeton, US*)
[77] Stobbs J.M., Tookey A., Thornton A.J. and Farley T. 2024 The infrared thermography system on the MAST-U tokamak *Rev. Sci. Instrum.* **95** 113509
[78] Herrmann A., Junker W., Gunther K., Bosch S., Kaufmann M., Neuhauser J., Pautasso G., Richter T. and Schneider R. 1995 Energy flux to the ASDEX-Upgrade diverter plates determined by thermography and calorimetry *Plasma Phys. Control. Fusion* **37** 17–29
[79] O'Gorman T., Naylor G., Scannell R., Cunningham G., Brunner K.J., Martin R. and Croft D. 2014 Design of a real-time two-color interferometer for MAST Upgrade *Rev. Sci. Instrum.* **85** 11D861
[80] Coutlis A., Bandyopadhyay I., Lister J.B., Vyas P., Albanese R., Limebeer D.J.N., Villone F. and Wainwright J.P. 1999 Measurement of the open loop plasma equilibrium response in TCV *Nucl. Fusion* **39** 663–83
[81] van Berkel M., Kobayashi T., Vandersteen G., Zwart H.J., Igami H., Kubo S., Tamura N., Tsuchiya H. and De Baar M.R. 2018 Heat flux reconstruction and effective diffusion estimation from perturbative experiments using advanced filtering and confidence analysis *Nucl. Fusion* **58** 096036